

ÉCOLE POLYTECHNIQUE FÉDÉRALE DE LAUSANNE

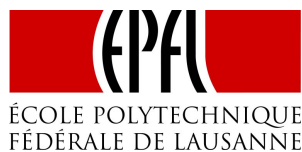
SEMESTER PROJECT REPORT

# Identification and Control of a High Power Rocket

*Hassan Arif*

Professor **Collin Jones**

Supervisor **Diwale Sanket Sanjay**



ÉCOLE POLYTECHNIQUE  
FÉDÉRALE DE LAUSANNE

June 22, 2017

## Contents

<b>1</b>	<b>Introduction</b>	<b>2</b>
<b>2</b>	<b>Model Rocket flight</b>	<b>3</b>
<b>3</b>	<b>Aerodynamic Model for a Rocket</b>	<b>5</b>
3.1	Normal Force . . . . .	6
3.2	Center of Pressure Location . . . . .	8
3.3	Damping parameters . . . . .	9
3.4	Drag Coefficient . . . . .	10
3.5	Control Surfaces . . . . .	12
3.5.1	Airbrake model . . . . .	13
3.5.2	Aileron model . . . . .	14
<b>4</b>	<b>Six DOF Trajectory Simulator</b>	<b>15</b>
4.1	Simulator layout . . . . .	15
4.2	Flight Simulation . . . . .	16
4.3	Simulation Outputs . . . . .	19
4.4	Comparison with RockSim . . . . .	21
4.5	Monte Carlo Simulation . . . . .	22
<b>5</b>	<b>Modified Tethys with control Surfaces</b>	<b>24</b>
5.1	Ailerons . . . . .	26
5.2	Airbrakes . . . . .	27
5.3	Electronics . . . . .	28
5.4	Structure . . . . .	29
<b>6</b>	<b>Wind tunnel Testing</b>	<b>30</b>
6.1	Brake test analysis . . . . .	31
6.2	Aileron test analysis . . . . .	32
<b>7</b>	<b>Flight and Data Analysis</b>	<b>33</b>
7.1	RORO test flight . . . . .	34
7.2	Tethys test flight . . . . .	36
<b>8</b>	<b>Conclusion</b>	<b>38</b>

## 1 Introduction

Rockets demonstrate the most concentrated source of power of any human-made machine, a controlled explosion enabling us to leave the shackles of Earth's gravity. It is not surprising that they have inspired generations of engineers. Amateur rocketry started in the 1950s [6] when hobbyists, inspired by the gains in rocket technology, wanted to test their skills in building rockets. Rocketry was a relatively unsafe hobby at this time. However, over the years there have been considerable advances. Both in the availability of reliable commercially available parts and in the availability of information required to calculate the dynamics of rockets.

Recently, the advances in the commercial rocket industry has set off another wave of interest in rocket science. Perhaps due to this a team representing Switzerland was formed to participate at the Intercollegiate Rocket Competition (IREC) in June 2017 [18]. The team comprises of students from Swiss Federal Institute of Technology Lausanne (EPFL), Swiss Federal Institute of Technology Zurich (ETHZ) and University of Applied Sciences and Engineering of the Canton Vaud (HEIG). The aim was to build a high power rocket for the category "10,000[ft] ( $\approx 3000[m]$ ) apogee with commercial-off-the-shelf (COTS) solid motor". A high power rocket is defined as a rocket with the total impulse ranging from 160[Ns] to 40960[Ns] [3]. If these rockets carry some instrumentation for suborbital testing they can also be referred to as sounding rockets.

This semester project was proposed as a part of the IREC competition. The goal is to identify the aerodynamic characteristics of the rocket, while accounting for perturbations and uncertainties. To achieve this a 6 degree of freedom (DoF) simulator, for an axis-symmetric rigid body rocket, was built in MATLAB. An aerodynamic model constructed from semi-empirical equations was incorporated into this simulator. This simulator can predict the trajectory of the rocket and help design the passive stability characteristics of the rocket. To account for uncertainties the simulator is able to perform a Monte Carlo simulation by varying aerodynamic parameters and wind to obtain the height distribution. The simulator is also able to model the effect of control surfaces, i.e. air brakes and ailerons for controlled flight.

Secondly, active control schemes are investigated with the intent of enhancing the ability of the rocket to reach the apogee of 10,000[ft]. During the course of the build of the competition rocket (RORO1) it was decided to exclude active control from the rocket due to risk. Thus, a smaller rocket with actuated air brakes and ailerons was built for testing as a part of this project. Furthermore, To validate the simulator design and to obtain improved aerodynamic coefficients of the control surface, both the rockets were tested at the Geneva wind tunnel.

With the help of the Advance Rocketry Group of Switzerland, both the competition rocket (RORO1) and the smaller test rocket with open loop braking were successfully tested. The flight data from both of these flights is analyzed and compared with the simulator.

Beyond the semester project the aim is to provide an open source in-house simulator for usage by the following years' IREC teams. Secondly, to create a strong starting point upon which future investigations can be built -especially, in the area of attitude control and braking.

## 2 Model Rocket flight

The flight of a model rocket is described in this section with specific reference to RORO1, the rocket which will fly at IREC 2017, and the modified level 1 rocket, Tethys. A model rocket flight can be split into 4 phases: Launch, Powered flight, coasting phase and recovery. (Figure 1).

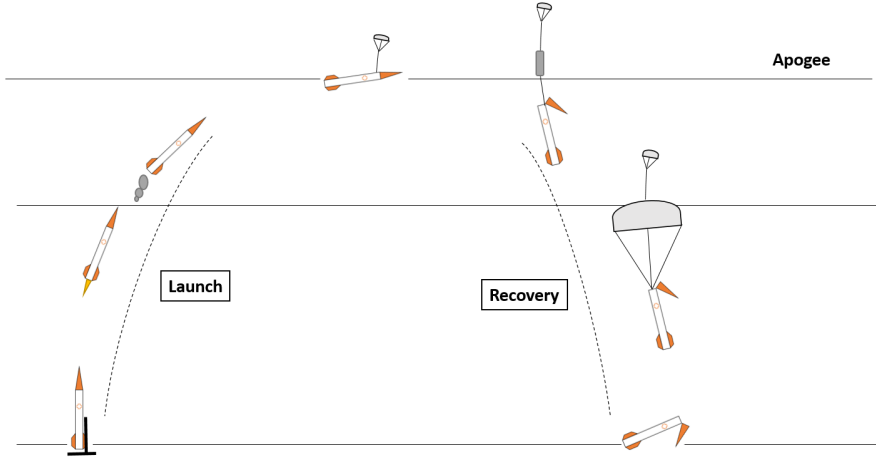


Figure 1: Phases of flight in a model rocket

During launch phase the rocket motor is ignited. Since most model rockets are only passively stable with the airflow over the fins providing most of the stability. The rocket is attached to a launch rail during the launch phase so they can gain the velocity needed to provide stabilizing moments. For IREC the rail is 5,5 meters long and launch angle is 84 degrees. The rail exit velocity is an important parameter in selecting the motor. It should be high enough such that the rocket is stable and not significantly affected by wind. During powered flight the motor accelerates the rocket to its top speed. This is around 0.8 Mach for RORO1 in competition configuration, with a burn time of 3.6[s]. Aerodynamic forces provide stabilizing moments and try to keep the flight angle of attack close to zero. The duration of this phase depends on the rocket size and thus the class of motor installed in the rocket.

During the coasting phase only the aerodynamic forces and gravity are acting on the rocket. The rocket decelerates till the vertical velocity reaches zero, for RORO1 this is approximately 25[s] after launch. At this stage the parachute is deployed, usually the rocket body splits and the parachute is pulled out. There are various methods to deploy the parachute. In RORO1 this is deployed by a recovery system that detects the altitude through an altimeter and deploys high pressure  $CO_2$  cartridge to deploy the parachute. For smaller rockets, like the level 1 rocket, this is done by a delay fuse and an explosive charge. After parachute deployment, the rocket descends with the help of either a 2 phase system with smaller drogue and a main parachute like RORO1, or just one parachute for the level 1 rocket.

Motor class is designated by letter from A to O, having the highest total impulse [9]. The rocket motor used for RORO1 is a M2400 motor with a total impulse of 7400Ns (Figure 2). The smaller Tethys has a H243 motor with a total impulse of 230Ns. These are solid motors consisting of a mix of ammonium per-chlorate and powdered aluminium [6]. Alternate to these are hybrid motors powder my a liquid oxidizer and a solid fuel mix. Typically, passively controlled rockets fly up to 5km.

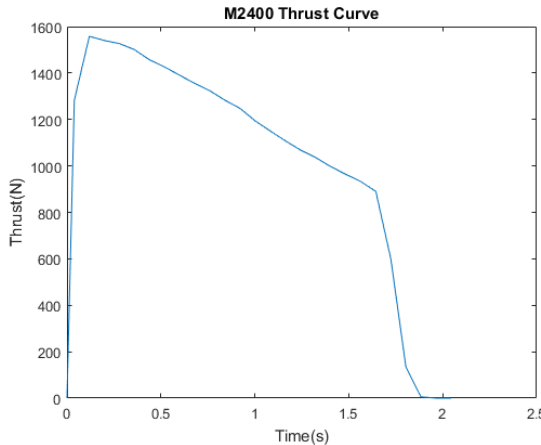
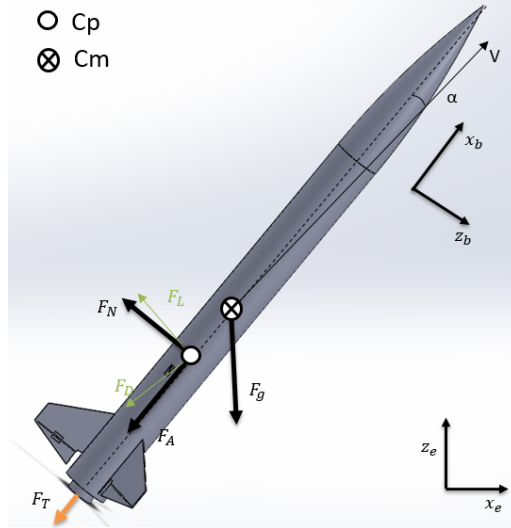


Figure 2: The thrust curve of the M2400 motor [9]

The flight dynamics of a model rocket are similar to any rocket. There are 3 forces that act on a rocket. Thrust, gravitational force and aerodynamic forces as seen in Figure 3. The gravitational force and the thrust acts at the center of mass of the rocket. The sum of aerodynamic forces act on the center of pressure of the rocket, and in turn produce a moment about the center of mass. The aerodynamic forces can be divided in to lift ( $F_L$ ) and drag forces ( $F_D$ ). These forces are perpendicular to each other with the drag pointing in the opposite direction of the velocity vector. In model rocketry it is more convenient to describe the forces in the frame of the rocket, as the normal forces ( $F_N$ ) and axial forces ( $F_A$ ). This notation will be used through this report. The procedure to calculate the magnitude of these forces are described in Section 3.

Figure 3: Forces on a rocket,  $F_N$  and  $F_A$  act at the center of pressure (Cp) and  $F_T$  and  $F_g$  act at the center of mass(Cm). Angle of attack is between velocity(V) of the Cp of the rocket and the rocket axis.

Rocket stability is determined by the direction of the moment created by the normal forces. The magnitude and location of this force is a function of the angle of attack ( $\alpha$ ) of the rocket. As long as the center of pressure is located aft of the center of gravity (Cp and Cm in Figure 3), the normal forces will produce a stabilizing moment, and attempt to reduce the angle of attack. The distance between the center of mass and the center of pressure is called the stability margin. In model rocketry stable rockets usually maintain a low angle of attack.

The mass and inertia of the rocket change during flight as the propellant is burnt. This also results in a change in the center of mass location. Thus, while designing a stable rocket this has to be taken into account. For IREC and for model rocketry in general. It is recommended that the stability margin stays

between 1 and 2 calibers, where 1 caliber is the diameter of the rocket.

The center of pressure moves up towards the center of mass if the angle of attack is increased. If the stability margin is too low, the  $C_p$  might move beyond the  $C_m$  destabilizing the rocket. If the rocket is too stable it tends to head into the wind, as the wind causes a nonzero angle of attack. This effect is especially prominent when exiting the rail. At this point the magnitude of the wind with respect to the rockets rail exit velocity is high, causing a relatively large angle of attack. The over-stable rocket will attempt to rotate into the wind. Due to the high correcting moment the rocket can over-rotate and become unstable. This phenomena is called weather cocking.

### 3 Aerodynamic Model for a Rocket

Modelling the forces correctly is vital to the accuracy of a simulator. The effect of aerodynamics forces is the hardest to determine between the 3 forces acting on the rocket. In the field of aerodynamics its is generally hard to compare the absolute magnitude of forces. Aerodynamic forces are converted to dimensionless coefficients normalized by the dynamic pressure  $\frac{1}{2}\rho_0^2$  and the reference area  $A_{ref}$ , this is taken as the cross-section of the body tube for a rocket.

$$C_i = \frac{F_i}{\frac{1}{2}\rho_0^2 A_{ref}} \quad (1)$$

$$C_m = \frac{m}{\frac{1}{2}\rho_0^2 A_{ref} d} \quad (2)$$

where  $F_i$  is the aerodynamic force and the  $m$  is the aerodynamic moment acting on the rocket. Aerodynamic forces can be split into pressure forces, caused by the fluid impacting the surface of the rocket and by viscous forces due to the friction between the fluid and the rocket. The coefficients are functions of the Reynolds number and angle of attack, for velocity greater than Mach 0.4 compressibility of flow starts playing a significant role, they are also a function of the Mach number.

$$C_i = f(\alpha, Re, M) \quad (3)$$

Analytical solutions to determine these forces exist only in very specific cases. More generally, like in the case of rocket flight, these coefficients are determined by semi-empirical equations determined using flow theory and experimental testing, and is a function of various parameters as seen in 3. In this report the focus will be on the subsonic region below Mach 0.8. At this velocity the compressibility of air has to be taken into account.

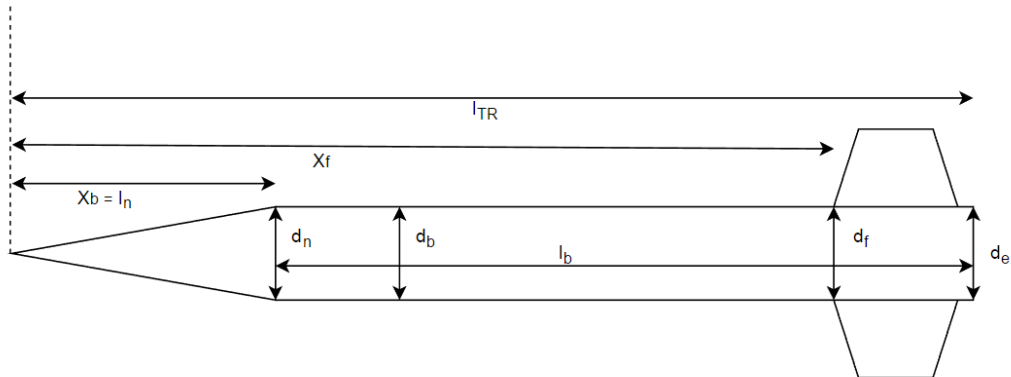


Figure 4: Schematics of a general rocket design with total length  $l_{TR}$

Figure 4 shows the layout of a standard rocket. In the case of both RORO1 and Tethys, the boattail, the conic structure at the tail of the rocket, is not present. Furthermore, the diameter along the length of

the rocket body ( $l_b$ ) does not vary (i.e.  $d = d_n = d_b = d_f = d_e$ ).  $X_b$  denotes the starting location of the cylindrical body tube and  $X_f$  is the starting location of the fins. The morphology of the fin is detailed in Figure 6.

### 3.1 Normal Force

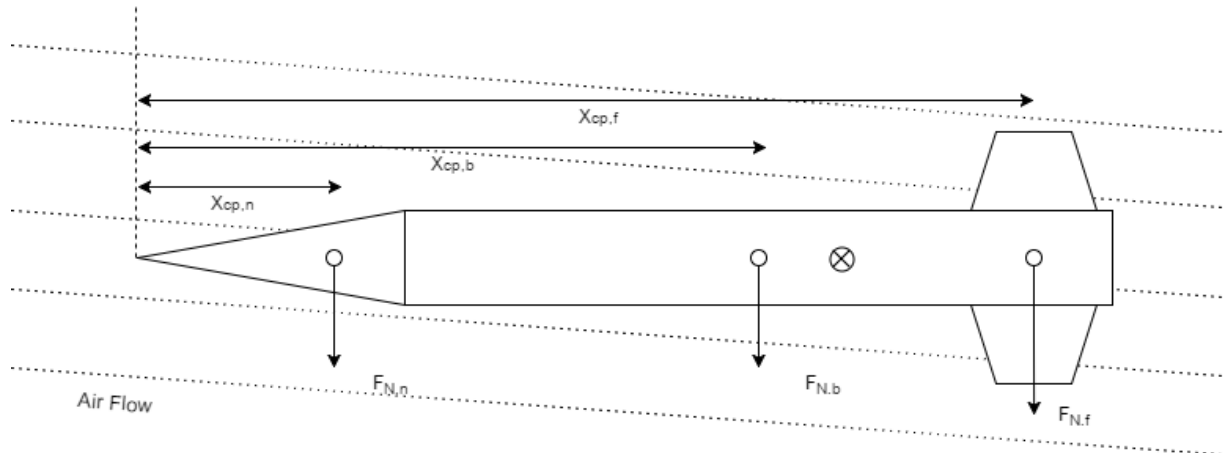


Figure 5: Normal forces acting on the center of pressures of the individual sections of the Rocket.  $F_{N,n}$  on the nose cone,  $F_{N,b}$  on the body tube and  $F_{N,f}$  on fins

The method laid out by Barrowman in [1] is generally used to calculate the normal forces acting on a model rocket. The calculations are valid under the following assumption:

- The angle of attack is close to zero ( $< 10 \text{ deg}$ )
- Speed much lower than the speed of sound
- No rapid change of flow
- Smooth nose cone ending on a point
- Axis symmetric rocket
- Thin fins compared to the rest of the body

Over the years enhancements have been made to the Barrowman method to account for compressibility of air at higher speed and the lift forces generated by the body as proposed by Galejs [5]. Also to enhance accuracy some small angle approximations are removed [6]. These equations are presented here. The normal force coefficient  $C_N$  is a function of  $\alpha$  and for small angles can be approximated as a linear function.

$$C_N = C_{N_\alpha} \alpha \quad (4)$$

where  $C_{N_\alpha}$  is a first order derivative  $\frac{\partial C_N}{\partial \alpha}$ , and is sometimes called the stability derivative. This is calculated for each section of the rocket and then summed to find the total forces as seen in Eq. 5. We will focus only on the nose cone the body tube and the fins, as these are the most relevant in our case. For boat-tails and conic sections, both Barrowman [1] and Mandell [2] are good sources.

$$C_{N(Rocket)} = \sum C_{N(Part)} \quad (5)$$

The normal force at a location  $x$  on the section of the body are at subsonic flow are given by

$$N = \rho v_0 \frac{\partial [A(x)w(x)]}{\partial x} \quad (6)$$

where  $A(x)$  is the cross section of the body and  $w(x)$  is the local down-wash

$$w(x) = v_0 \sin(\alpha). \quad (7)$$

Equations 6 and 7 are substituted in Eq. 1 and integrated over the length of the body resulting in Eq. 8, which only depends on the end areas of a body section.

$$C_{N_\alpha} = \frac{C_N}{\alpha} = \frac{2}{A_{ref}} [A(l) - A(0)] \frac{\sin(\alpha)}{\alpha} \quad (8)$$

The fraction  $\frac{\sin(\alpha)}{\alpha}$  is a result of not assuming a small angle approximation of the down-wash in Eq. 6. If this approximation is taken the fraction disappears and the result becomes equivalent to Barrowman original derivation.

For larger but especially longer rockets, the lift generated by the cylindrical body-even at small angles of attack- cannot be neglected. Galejs[5] proposes a correction term (Eq.9) which adds on to the  $C_{N_\alpha}$  to account for this.

$$C_{N_\alpha \text{bodylift}} = K \frac{A_{plan}}{A_{ref}} \frac{\sin^2(\alpha)}{\alpha} \quad (9)$$

$A_{plan} = d.l$ , i.e. the platform area for a cylinder, and  $K \approx 1.1$ . Again the small angle approximation of  $\alpha^2 \approx \sin^2(\alpha)$  is dropped here. It is also assumed that the body force for non cylindrical parts can be approximated by this equation, and the force is applied at the center of the platform area (Eq.18 and Eq. 19 ).

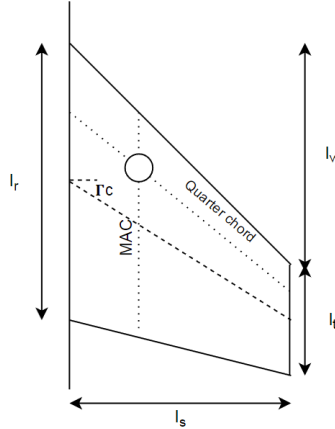


Figure 6: Trapezoidal fin with the center of pressure represented by the circle

The normal force coefficient of a single fin is derived by Barrowman using Diederich's [10] semi-empirical method based on thin airfoil theory. Here, only the final result is presented.

$$(C_{N_\alpha})_1 = \frac{2\pi \frac{l_s^2}{A_{ref}}}{1 + \sqrt{1 + (\frac{\beta s^2}{A_{fin} \cos(\Gamma_c)})^2}} \quad (10)$$

where the compressibility correction is given Eq. 11 and  $\Gamma_c$  is the mid chord sweep angle (Figure 6)

$$\beta = \sqrt{M^2 - 1} \quad (11)$$

The sum of the normal moment for 3 or more axially symmetric fins can be approximated to be the same at any roll angle of the rocket. For 3 and 4 fins Barrowman makes the derivation as shown in

Eq. 12, where  $n$  is the number of fins. For more fins Openrocket [6] extends this derivation. However, it is not presented here as RORO1 had 3 fins, and most conventional models rockets go up to 4 fins.

$$(C_{N_\alpha})_n = \frac{n}{2} (C_{N_\alpha})_1 \quad (12)$$

These forces have to be corrected for the effect on the normal forces of the fins due to the presence of the body. The effect of the fins on the body can be ignored due to the much smaller magnitude. This is given by

$$(C_{N_\alpha})_{fins} = K_{T(B)} (C_{N_\alpha})_n \quad (13)$$

Where  $K_{T(B)}$  is approximated by Barrowman as Eq. 14. Here  $r_t$  is the body radius.

$$K_{T(B)} = 1 + \frac{d_b}{2l_s + d_b} \quad (14)$$

These equations are implemented in the simulator to calculate the rocket normal forces.

### 3.2 Center of Pressure Location

The center of pressure  $X_{cp}$  of the rocket can be calculated as a weighted sum the center of pressure of the individual components  $X_i$ . Where  $X$  is the distance from the front of the nose cone (Figure 5).

$$X_{cp} = \frac{\sum X_i (C_{N_\alpha})_i}{\sum (C_{N_\alpha})_i} \quad (15)$$

In most rockets an ogive-shaped nose is used, the center of pressure location for the nose cone is given by Eq.16. This can be derived from equating the normal forces with the rotation moments by those forces about the tip of the cone [6]. For the fins at low subsonic speeds it is located on quarter length of the mean aerodynamic chord(MAC) [1]. For trapezoidal fins this location can be resolved geometrically as shown in Eq. 17 (Figure 6).

$$X_{cp,n} = 0.466l_n \quad (16)$$

$$X_{cp,f} = X_f + \frac{l_m(l_r + 2l_t)}{3(l_r + l_t)} + \frac{1}{6} \left[ l_r + l_t - \frac{l_r l_t}{l_r + l_t} \right] \quad (17)$$

Furthermore, the body lift correction  $C_{N_\alpha bodylift}$  from Eq.(9) is applied to the center of the platform area of the part, (i.e the ogive nose cone and the body tube).

$$X_{platfrom,n} = \frac{5}{8}l_n \quad (18)$$

$$X_{platfrom,b} = X_b + \frac{1}{2}l_n \quad (19)$$

Equations 16 to 19 are substituted in Eq. 15 along with the appropriate  $C_{N_\alpha}$  to get the center of pressure of the rocket.

### 3.3 Damping parameters

External perturbations like wind, the launch-rail rocket contact forces, misalignment of thrust with the center of mass and misalignments of structural elements like fins can cause pitch oscillations and roll in a rocket. A well designed rocket will dampen these oscillations. It is important to be able to estimate these damping parameters to be able to predict the performance of the rocket.

Pitch damping can be split into two components. Thrust damping, provided by the thrust of the motor, caused by the momentum of the mass being ejected from the nozzle. Aerodynamic damping, caused by the lateral velocity of the oscillating rocket. Mandell [2] provides a detailed derivation of the pitch moment damping parameters shown in equation (20) for aerodynamic damping and equation (21) for thrust damping. It is to be noted that these parameters are not dimensionless coefficients.

$$C_{2,aerodynamic} = \frac{\rho}{2} v^2 A_{ref} ((C_{N,n}(X_{cp,n} - X_{cm,n})^2 + (C_{N,b}(X_{cp,b} - X_{cm,b})^2 + (C_{N,f}(X_{cp,f} - X_{cm,f})^2)) \quad (20)$$

$$C_{2,thrust} = \dot{m}(l_{cn}^2 - l_{cc}^2) \quad (21)$$

where  $l_{cn}$  is the distance from the center of mass to nozzle exit and  $l_{cc}$  is the distance from the center of mass of the rocket to the center of mass of the propellant.

If the rocket starts to rotate, the fin encounters air at a certain angle of attack ( $\eta_i$ ). This angle increases radially outwards from the center. The angle of attack causes an opposing force on the fin, which in turn causes a damping. This is derived by Niskanen [6] by calculating the force (Eq 22) of the flow on a thin section of a fin ( $c_i \Delta \xi_i$ ) rotating at an angular velocity  $\omega$  and integrating it outwards. For  $N$  fins the damping coefficient is given by Eq. 23.

$$F_i = C_{N_{\alpha 0}} \frac{1}{2} \rho_0^2 c_i \Delta \xi_i \eta_i \quad (22)$$

$$C_{rd,f} = \frac{NC_{N_{\alpha 0}} \omega}{A_{ref} dv_0} \sum c_i \xi_i \Delta \xi \quad (23)$$

where  $N$  is the number of fins,  $C_{N_{\alpha 0}} = \frac{2\pi}{\beta}$  is the lift coefficient of thin airfoils according to potential flow theory with  $\beta$  for compressibility correction.  $\sum c_i \xi_i \Delta \xi$  represents the integral of a thin strip of the fin integrated radially outwards along the span of the fin. For trapezoidal fins the integral can be evaluated as,

$$\sum c_i \xi_i \Delta \xi = \frac{l_r + l_t}{2} \left( \frac{d_f}{2} \right)^2 l_s + \frac{l_r + 2l_t}{3} \left( \frac{d_f}{2} \right) l_s^2 + \frac{l_r + 3l_t}{12} l_s^3. \quad (24)$$

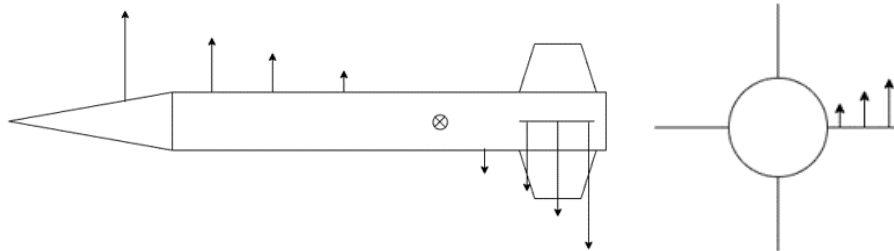


Figure 7: Illustration of pitch and roll damping forces

### 3.4 Drag Coefficient

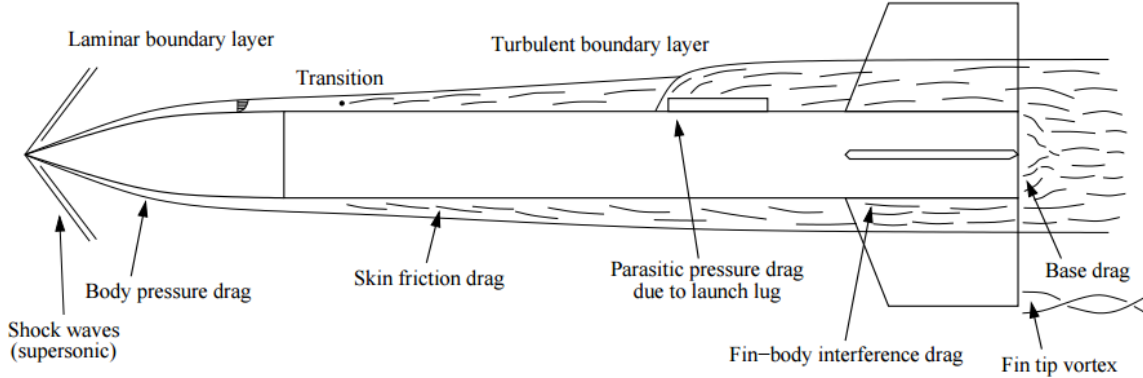


Figure 8: Various sources of drag during the flight of a rocket [6]

The drag forces by a rocket during flight are shown in Figure 8. Since only subsonic flight is considered the effect of the shock wave is ignored. Body pressure drag is caused by the flow being forced around the forebody of the rocket (i.e the nose cone and the body tube). As the air flows goes around the rocket, the layers closest to the rocket stick to the rocket. This is the skin friction drag and is caused by the viscous flow of the fluid around the rocket, it is also known as viscous drag. The velocity of this flow, relative to the rocket, increases further away from the rocket, reaching free stream velocity. This area of velocity gradient of the flow is the boundary layer around the rocket. This boundary layer can be laminar or turbulent depending on the Reynold number of the flow. The transition occurs around  $Re$  of  $10^5$  [2], beyond which the flow is considered turbulent. For much of the flight, the rocket's velocity is high enough to primarily have a turbulent boundary layer. However, there is a region at the front of the rocket where the  $Re$  is lower than the critical amount at the boundary layer can be considered laminar. As the rocket gains speed, this transition moves closer to the tip of the nose cone. Both the forebody and the fins have skin friction drag. The magnitude of this drag is affected by surface roughness.

At the rear of the rocket the flow separates and recombines further down stream. This separation of flow behind the rocket creates an area of low pressure and flow recirculation. This low pressure causes drag on the rocket and is known as base drag. The fins disturb the air flow over the forebody and cause some amount of drag. Furthermore, the fins can shed vortices from their tips. Vortices are oscillating flow, the energy required to create these oscillations is taken from the momentum of the rocket, thus causing Vortex shedding is not directly modelled simulator.

Lastly, launch lugs, and other protruding features of the rocket cause parasitic drag. Which is a combination of pressure, base and friction drag of these features. Mandell [2] gives estimates and derivation of the contribution of the various sources of drag, Box al et.[3] effectively summarizes these in a compact and clear manner. The estimated contributions of various sources as follows:

- Launch lugs up to 35% of total  $C_d$ ;
- Skin friction of forebody, 25% to 30%;
- Skin friction of fins, 25% to 30%;
- Base drag up to 10%;
- Pressure drag less than 1%.

The coefficient provided by Mandell are derived using USAF DATCOM method which gives semi-empirical formulas to derive drag. First, the drag at zero angle of attack is calculated, this is then expanded to higher angles of attack.

**Body Drag** on the forebody is given by the Eq. 25.  $l_b$  is the length of the boat-tail, which in case of ROR01 an Tethys is zero.  $C_{f(fb)}$  is the skin friction drag of the forebody. The various lengths are illustrated in Figure 4.

$$C_{D,fb} = \left[ 1 + \frac{60}{l_{TR}/d_b} + 0.0025 \frac{l_b}{d_b} \right] \left[ 2.7 \frac{l_n}{d_b} + 4 \frac{l_b}{d_b} + 2 \left( 1 - \frac{d_d}{d_b} \right) \frac{l_c}{d_b} \right] C_{f,fb}. \quad (25)$$

**Base Drag** is given by Eq. 26.

$$C_{D,b} = 0.029 \frac{\left(\frac{d_d}{d_b}\right)^3}{\sqrt{C_{D,fb}}} \quad (26)$$

**Fin Drag** is given by Eq. 27.  $C_{f,f}$  is the skin friction drag of the fins.  $A_{fp}$  is the platform area of the fins defined as  $A_{fp} = A_{fe} + \frac{1}{2}d_f l_r$ , where  $A_{fe} = \frac{1}{2}(l_r + l_s)l_s$  is the exposed area of the trapezoidal fin and the second term is the virtual extension of this fin to the central rocket axis.

$$C_{D,f} = 2C_{f,f} \left( 1 + 2 \frac{T_f}{l_m} \right) \frac{4N(A_{fp})}{\pi d_f^2} \quad (27)$$

**Interference Drag** is given in Eq. 28.

$$C_{D,i} = C_{f,f} \left( 1 + 2 \frac{T_f}{l_m} \right) \frac{4N(A_{fp} - A_{fe})}{\pi d_f^2} \quad (28)$$

**Viscous friction** or skin friction is given by Eq. 29. The  $Re_c$  is taken as  $10^5$ , this is the laminar to turbulent transition, below this the flow is considered laminar. The rocket normally has a short region of laminar flow followed by a transition of turbulent flow (Figure 8), this transition is defined by  $B$ . To calculate the viscous drag of the forebody  $C_{f,fb}$ , the characteristic dimension for calculating the Reynolds number is taken as  $l_{TR}$ , the total rocket length. For the fins,  $C_{f,f}$ , the length is taken as  $l_m$ , the mean chord length of the fin.

$$C_f = \begin{cases} \frac{1.328}{\sqrt{Re}} & \text{if } Re \leq Re_c \\ \frac{0.074}{Re^{0.2}} - B \frac{1.328}{\sqrt{Re}} & \text{if } Re \geq Re_c \end{cases} \quad (29)$$

where

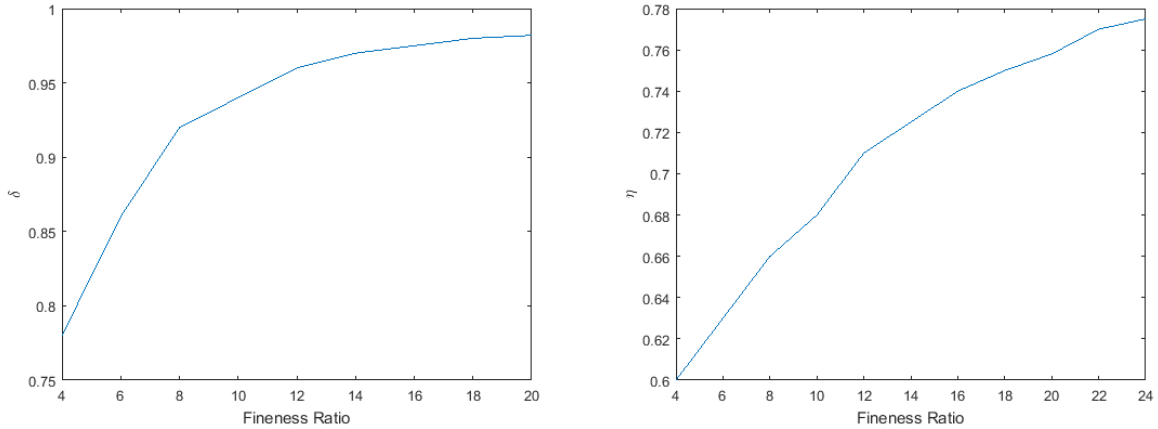
$$B = R_c \left( \frac{0.074}{Re^{0.2}} - \frac{1.328}{\sqrt{Re}} \right) \quad (30)$$

**Launch lug** is approximated as a pin protruding from flat surface. The drag is taken as approximately 0.8, using the frontal area of the pin as the reference area. [15]p. 5-8.

**Total Drag** is the sum of the various sources (Eq. 31). All drag coefficients have to be normalised to the rocket reference are  $A_{ref}$  before being summed. For this case it only applies to the launch lugs.

$$C_D = C_{D,fb} + C_{D,fb} + C_{D,b} + C_{D,f} + C_{D,i} + C_{D,lug} \quad (31)$$

**Drag at angle of attack** has to be considered during rocket flight. This can be divided to  $C_{Db(\alpha)}$  drag due to body (Eq. 32) and  $C_{Df(\alpha)}$  drag due to fin sets (Eq. 33).  $\delta$  (Mass ratio) and  $\eta$  (ratio of drag of an infinite length cylinder to a finite length cylinder) are determined from wind tunnel experiments as a function of the fineness ratio ( $\frac{l_b}{d}$ ) and show in Figure 9. These factors are described in more detail in Mandell ([2] p. 408).

Figure 9:  $\delta$  and  $\eta$  as functions of the fineness ratio [2]

$$C_{Db(\alpha)} = 2\delta\alpha^2 + \frac{3.6\eta(1.36l_{TR} - 0.55l_n)\alpha^3}{\pi d_b} \quad (32)$$

$$C_{Df(\alpha)} = \alpha^2 \left[ 1.2 \frac{4A_{fp}}{\pi d_f^2} + 3.12(k_{fb} + k_{bf} - 1) \frac{4A_{fe}}{\pi d_f^2} \right] \quad (33)$$

$k_{fb}$  and  $k_{bf}$  are the coefficients of fin-body and body-fin interference respectively. They are defined in Eq. 34 and 35 as a function of  $R_s = \frac{d_b}{2l_s + d_b}$

$$k_{fb} = 0.8065R_s^2 + 1.1553R_s \quad (34)$$

$$k_{bf} = 0.1935R_s^2 + 0.8174R_s + 1 \quad (35)$$

The angle of attack drag contributions can be added on to the zero alpha drag (Eq. 36).

$$C_D = C_{D(0)} + C_{Db\alpha} + C_{f(\alpha)} \quad (36)$$

For the simulation we are interested in the axial drag,  $C_A$ , as Barroman's method provides  $C_N$  and not lift. We have to take the axial component of  $C_D$ , using the known value of  $C_N$ .

$$C_A = \frac{C_D \cos(\alpha) - \frac{1}{2} C_N \sin(2\alpha)}{1 - \sin^2(\alpha)} \quad (37)$$

Finally,  $C_A$  is corrected for the compressibility of air.

$$C_{A,corrected} = \frac{C_A}{\beta} \quad (38)$$

### 3.5 Control Surfaces

There are two types of control surfaces to be modelled. Air brakes, which be seen as plates that come out from the rocket body increasing the drag coefficient. Ailerons, which are moving parts on the fins which redirect the airflow causing pitching and rotational moments. The brake and aileron models have been developed using Hoerners books on Fluid Dynamic Lift [15] and Fluid Dynamics Drag [14]. These books provide an in depth insight on these topics. The reference area for the brake coefficients is the surface area of a flat plate, for the fin this is the surface area of the fin. To get the coefficients with respect to the rocket these have to be normalized to the rocket reference area.

$$C_{rocket} = \frac{A_{ref, controlsurface}}{A_{ref}} C_{controlsurface} \quad (39)$$

### 3.5.1 Airbrake model

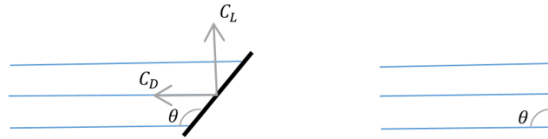


Figure 10: Left, The normal forces of a plate at an angle to the air flow split into Lift and Drag forces; Right, a 3 dimensional plate perpendicular to flow with  $C_{D0} = 1.17$

The air-brakes can be approximated by plates in air flow. According to numerous wind tunnel tests the drag coefficient of a plate perpendicular to the air flow is almost constant at  $C_{D0} = 1.17$  up to a Reynolds number of  $10^7$  ([14] p. 3-15). Which is convenient as most of model flight takes place within this range. This drag value only holds for plates with an aspect ratio close to 1, as the aspect ratio decreases the  $C_{D0}$  approaches 1.98, which is close to the theoretical value of 2 for 2 dimensional plates (i.e. with infinite depth, zero aspect ratio). The normal force coefficient for plates at a certain angle of attack with respect to the air flow is given by Eq. 40 ([14] p. 7-17), where  $k = 2$  from theory. This equation is derived from Newtonian impact of the flow on to the plate, where all the momentum of flow is transferred to the plate. Eq. 40 is for zero aspect ratio plates (2 dimensional plates). For a 3 dimensional plates  $k$  can be replaced by  $C_{D0} = 1.17$ . This equation is only valid for separated flow, which is true for air brakes attached to the rocket surface. The lift and drag coefficients (as seen in Figure 10, Left) for a 3 dimensional plate are given by Eq. 41 and Eq. 42 respectively.

$$C_{N\theta} = k \sin^2(\theta) \quad (40)$$

$$C_{D\theta} = C_{D0} \sin^3(\theta) \quad (41)$$

$$C_{L\theta} = C_{D0} \sin^2(\theta) \cos(\theta) \quad (42)$$



Figure 11: Air-brakes schematic showing the boundary layer intersecting the brake surface

To get a better estimate of the brake forces, the effect of the rocket body has to be accounted for. The boundary layer of the rocket body intersects the brake surfaces (Figure 11). This causes some momentum loss, which can be considered to be concentrated at the lower 25% of the boundary layer [14] p. 8-3. This loss in the dynamic pressure can be expressed as a ratio given by Eq. 43. Where  $\delta$  is the turbulent boundary layer thickness, given by Eq. 44 [16]. Where  $x$  is the distance from the start of the stagnation point, in this case the tip of the rocket. And  $Re_x$  is the Reynolds number with  $x$  as the characteristic length.

$$\frac{q_{eff}}{q} = (1 - 0.25 \frac{\delta}{h}) \quad (43)$$

$$\delta \approx \frac{0.37x}{Re_x^{0.25}} \quad (44)$$

The  $C_{D0}$  of the air brake can be corrected by the ratio in Eq. 43 to get the final drag coefficient of the brake as a function of the brake actuation angle.

$$C_{D\theta,corrected} = C_{D0}(1 - 0.25 \frac{\delta}{h}) \sin^3(\theta) \quad (45)$$

When the rocket is flying at a zero angle of attack the lift forces of the asymmetrically places brakes cancel. However, when the rocket is flying at a non zero angle of attack, the brake plate angles with respect of the flow are not the same for all the brakes, the magnitude of the lift forces is non zero. This has to be accounted for as normal force on the rocket. The force can be calculated as a vector sum of individual lift forces. The existence of this normal forces also mean that in order to have a stabilising moment the brakes have to be places close to but under the center of mass of the rocket.

### 3.5.2 Aileron model

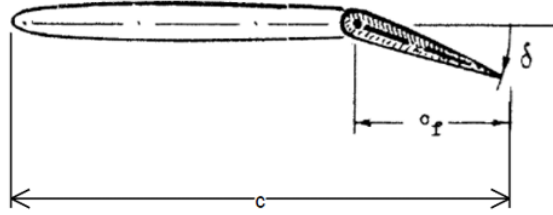


Figure 12: Cross-section of a wing with an aileron [15]

Ailerons deflect the air flow over the fins causing lift. This lift can be considered proportional to the angle of deflection  $\eta$  of the aileron for up to 15 degrees of deflection [15] p. 9-2.  $C_{L\alpha}$  of a thin fin can be calculated using Diederich's method [10] (Eq. 10 ) as was shown in Section 3.1 for calculating the normal forces contribution from the fins. With in this linear range of deflection of the aileron, a relation can found between lift generated at and angle of attack of the fin and the aileron deflection need to cancel that lift. The theoretical relation can be approximated by Eq. 46 [15]p. 9-2. Where  $\frac{c_f}{c}$  is the ratio of the chord length of the aileron to the chord length of the fin (Figure 12).  $\frac{d\alpha}{d\eta}$  is the effectiveness of the aileron. Eq. 46 gives the upper limit of this ratio. In reality there is a loss of effectiveness due to flow separation, the gap between the aileron and the fin and various other factors details of which can be found in [15].

$$\frac{d\alpha}{d\eta} = \sqrt{\frac{c_f}{c}} \frac{4}{\pi} \quad (46)$$

In this case the lift would be given by Eq. 47. Where the  $\alpha$  that provides the equivalent would be given by  $\frac{d\alpha}{d\eta}\eta$ .

$$C_L = C_{L\alpha} \frac{d\alpha}{d\eta} \eta \quad (47)$$

The induced drag due to lift can be calculated by Eq. 48, [14] p. 7-2.

$$C_D = C_L \tan\left(\frac{d\alpha}{d\eta}\eta\right) \quad (48)$$

## 4 Six DOF Trajectory Simulator

An in-house simulator was seen as an important step in prediction the dynamics and performance of the rocket. It gives the flexibility to customize the simulator to our application, beyond what can be achieved in available simulators. A stochastic element is also added to the simulation to get a probability distribution of the apogee height, and overall trajectories. Furthermore, it serves as a platform for testing control schemes.

A rocket simulation is simply the resolution of the generalized equations of motion under the defined external forces. In space any object has 6 degrees for freedom (DoF) for the rocket these are the Cartesian x, y, z and roll, pitch, yaw. A detailed derivation from first principles of these equations for an axis symmetric rocket are detailed by Siouris [11] in Chapter 2. Duncan and Endey implement these equations as a six degree of freedom simulator [12]. A much more recent implementation is done by Box et al. [3], using quaternions for a much more simplified implementation of the flight dynamics. It is assumed that the reader has a grasp over the quaternion representation of orientation and rates, information on this topic can be found in the lectures by H.Bleuler [13] .

### 4.1 Simulator layout

Following this reasoning a complete six degrees of freedom simulator was implemented in MATLAB to simulate the rocket. The simulator predicts the trajectory of the rocket by computing its various states at each time step. The simulator is based around a rocket class (`rocket.m`), environmental model (`environment.m`), aerodynamic models for drag(`Cd.m`) and normal forces (`Cn_alphaXcp.m`); and finally an ascent calculator (`accent_calc.m`) which was greatly influenced by the work done by Box et al.[4]. The implementation of the simulator is shown in Figure 13.

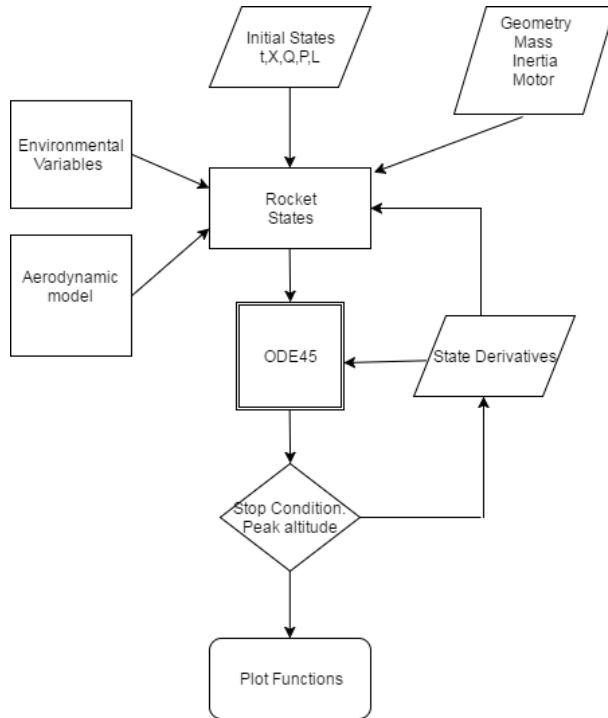


Figure 13: Flow chart of the implemented simulator

**The rocket class** stores all geometric data, inertial data, motor and thrust data and the relevant states of the rocket. The states, masses, inertias, center of mass and Reynolds number, stored in this class, are continuously updated during the rocket flight. The environment and aerodynamic models are both accessed through the rocket class. These models provide the environment variables and the aerodynamic coefficients at a given states of the rocket.

The state vector and the state derivatives of the rocket:

X Position in world coordinates

Q Orientation in quaternion

L Angular Momentum

P Linear Momentum

$\dot{X}$  Linear velocities

$\dot{Q}$  Angular velocities in quaternions

$\dot{L}$  Torques acting on  $X_{cm}$

$\dot{P}$  Forces acting on  $X_{cm}$

**The aerodynamic models** are the implementation of the equations described in Section 3. They are called through the rocket class at each time step of the rocket flight. `Cd.m` provides the axial drag coefficient and `Cn_alphaXcp.m` gives the stability derivative ( $C_{N_\alpha}$ ), the center of pressure location ( $X_{cp}$ ), damping parameters ( $C_{damping}$  and  $C_R$ ) and damping ratio ( $\zeta$ ).

The aerodynamic models can also be used separately to calculate the coefficients of drag and the normal forces and to analyze its dynamic and static stability.

**The environment model** takes various constants (Table: ) and calculates the air density, temperature, pressure, viscosity gravity and the speed of sound at given state in flight. These are calculated using the atmospheric model from the US Standard Atmosphere, 1976.[7]. A wind generator is also implemented in the environment model.

**The ascent calculator** takes the 6 degrees of freedom dynamical equations for the rocket and iteratively solves for the state derivatives then using the MATLAB ODE45 solver. ODE45 is an iterative solver which uses the Runge Kutta method and a varying time step to resolve the dynamical equations. Wind and velocity information is used here to calculate the angle of attack, this in turn determines the relevant aerodynamic coefficients for each state during flight.

## 4.2 Flight Simulation

As a first step the simulation is initialized. A variable for the rocket class is defined, during declaration an initialization function is called (`init_rocket.m`) which takes in an input text file, through which we can specify the properties of the rocket (Figure 14). This text file is the input interface for the user. It contains the complete geometry of the rocket , dry mass, center of mass inertias and motor type. The mass, inertias and  $X_{cm}$  are known to a high accuracy due to the detailed CAD model and measurements, thus specifying these quantities directly makes the simulation more representative of the real rocket.

```

Length,          2.626
Cone Length,    0.61
Diameter,       0.158
Number of Fins, 3
Fin height,     15e-2
Fin base length, 26e-2
Fin top length, 8e-2
Fin Sweep angle, 45
Fin thickness,   1e-2
Mass,           21.9
Ixx,            0.06452
Iyy,            9.191
Izz,            9.191
Xcm,            1.574
Launchpin height, 17e-3
Launchpin Dia,   30e-3
Rail angle,      84
AeroTech_M2400.eng, 0

```

Figure 14: Input data file for the simulator showing the launch configuration of RORO1, SI units

Next the motor is initialized `motor_init.m`, this takes the motor data from a `.eng` file and loads it to the rocket class. The `.eng` contain the thrust-time data of the motor (Figure 2) can be downloaded from [ThrustCurve.org](#) [9]. Finally, the environment model is created taking the Elevation[m], Temperature[C] and Pressure [Pa].

```

% Create rocket class
roro = rocket(init_rocket()); % creates class with the initial values
% Load rocket motor
motor_init( roro );
% Initialize Environmental variables
% optional argument: Elevation(m) Temperature(C) and Pressure(Pa)
env = environment(1400, 35, 86000, roro );

```

Figure 15: Example of the initialization sequence

After the initialization the ascent function is called. Using the ODE45 function of MATLAB its resolves the dynamical equation numerically. In input of the ODE45 function is a time vector and the initial state and state derivative vectors shown in Table . At each iteration the E.q50 to 67 are resolved. The effect of the launch rail is accounted for by constraining the rotational degrees of freedom until the magnitude of the distance travelled is greater than the launch rail length.

During the powered phase, the rocket changes its mass, inertia and  $X_{cm}$  due to the burning propellant. This is accounted for by the function `burn_data.m` inside the iteration loop. It is assumed that the total impulse generated is proportional to the total mass of the propellant, both of which are specified in the `.eng` thrust curve file. The geometry of the propellant is that of a hollow cylinder, and the dimensions are taken from the motor drawing, which are similar for a class of motors. When the motor is ignited, the inner walls burn and shift radially outwards (Figure 16). Each iteration the remaining mass of the propellant is calculated by the ratio in Eq. 49, updating the the total mass of the rocket. The  $X_{cm}$  of the rocket is also updated as propellant mass changes. Furthermore, the rate of change of mass is also calculated at this point, this is needed for calculating thrust damping. Using this remaining mass and the density of the propellant, the shift in the inner radius ( $R_{i,prop}$ ) can be calculated. With the new radius the inertia of the remaining propellant cylinder about the current rocket  $X_{cm}$  is calculated, updating the total rocket inertia.

$$\frac{M_{prop,remaining}}{M_{prop,total}} = \frac{Impulse_{prop,remaining}}{Impulse_{prop,total}} \quad (49)$$

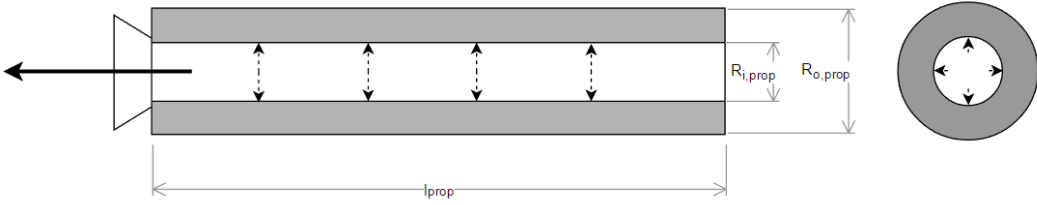


Figure 16: The hollow cylindrical shape of the propellant, the thrust direction shown by a solid arrow and the direction of changing radius due to the burn, dashed arrow

The following dynamical equations resolved at each iteration. The orientation  $Q$ , at the present state, can be converted to a rotational matrix  $R$ . This can be used to convert the roll, pitch and yaw axis from the rocket frame to the earth frame.

$$Y_E = RY_R$$

$$P_E = RP_R$$

$$R_E = RR_R$$

The velocity and angular rates in quaternion form are calculated.

$$\dot{\mathbf{X}} = \mathbf{P}/M \quad (50)$$

$$\omega = \mathbf{R}I^{-1}\mathbf{R}^T\mathbf{L}^T \quad (51)$$

Where is the rotation matrix  $R$  is used to transform the inertia matrix  $I$  from the rocket frame to the earth frame.  $\omega$  is the rotational velocity vector of the rocket in  $rads^{-1}$ . This is used to calculate the quaternion rates, using quaternion differentiation.

$$\mathbf{I} = \begin{bmatrix} I_{xx} & 0 & 0 \\ 0 & I_{yy} & 0 \\ 0 & 0 & I_{zz} \end{bmatrix}$$

$$\dot{\mathbf{Q}} = [\dot{s} \dot{\mathbf{v}}] \quad (52)$$

$$\dot{s} = \frac{1}{2}(\omega \cdot \mathbf{v}) \quad (53)$$

$$\dot{\mathbf{v}} = \frac{1}{2}(s\omega + (\omega \times \mathbf{v})) \quad (54)$$

To derive the axial and normal forces the relative coefficients are needed. These are a functions of the  $Re$ ,  $M$  and  $\alpha$  of the rocket at that state.  $Re$  and  $M$  are directly computed in the rocket class.  $\alpha$  is given by Eq 55. Where  $\hat{\mathbf{V}}$  is the normalized apparent velocity vector,  $\mathbf{V}$  and  $R_E$  is the roll axis of the rocket in the earth reference frame. The apparent velocity is the velocity of the center of pressure of the rocket.

$$\alpha = \cos^{-1}(\hat{\mathbf{V}} \cdot \mathbf{R}_E) \quad (55)$$

$\mathbf{V}$  can be calculated by Eq. 56. Where  $\mathbf{V}_{cm}$  is given by Eq. 57 and  $\mathbf{V}_\omega$  by Eq. 58.

$$\mathbf{V} = \mathbf{V}_{cm} + \mathbf{V}_\omega \quad (56)$$

$$\mathbf{V}_{cm} = \dot{\mathbf{X}} + \mathbf{W}; \quad (57)$$

$$\mathbf{V}_\omega = \bar{X}[\cos^{-1}(\mathbf{R}_E \cdot \hat{\omega})](\mathbf{R}_E \times \omega) \quad (58)$$

$\mathbf{V}_{cm}$  is the velocity about the center of mass;  $\mathbf{W}$  is the wind speed vector and  $\mathbf{V}_\omega$  is the rotational velocity component of the center of pressure about the center of mass of the rocket due to the  $\omega$  of the rocket. Here  $\bar{X} = [X_{cp} - X_{cm}]$  is the stability margin. It is important to note that the calculation of  $\alpha$

in the current state requires the knowledge of  $X_{cp}$  of that state. Which is self is a function of  $\alpha$ . If the angular rotation of the rocket is not large the  $X_{cp}$  of the previous time step can be used to calculate the  $\alpha$ . If the angular rotation is large, the  $\alpha$  estimate can be used to calculate a new  $X_{cp}$  and in turn  $\alpha$  iteratively. Alternatively,  $X_{cm}$  of the current state can also be used if the rotational rates of the rocket are low.

The total forces vector equates to the rate of change of the linear momentum and are given by the thrust, the gravitational force, the axial forces and the normal forces, Eq. 59. The force vectors are applied to the rocket in the earth frame of reference. Gravitational and thrust forces act on the center of mass, the aerodynamic forces act on the center of pressure. The thrust  $T$  is obtained from the motor thrust curve, is applied along the roll axis of the rocket. The gravity force is applied to earth down direction.

$$\dot{\mathbf{P}} = \mathbf{F} = \mathbf{F}_T + \mathbf{F}_g + \mathbf{F}_A + \mathbf{F}_N \quad (59)$$

$$\mathbf{F}_T = T\mathbf{R}_E \quad (60)$$

$$\mathbf{F}_g = [0, 0, -Mg]^T \quad (61)$$

Once the  $\alpha$  is known the axial, normal, and damping coefficients for the state can be calculated.  $F_N$  and  $F_A$  are given by Eq. 62 and 63. The axial force vector is applied in the direction of the roll axis ( $\mathbf{R}_E$ ) and this includes the contribution from air-brakes . The normal force vector is applied orthogonal to the roll axis ( $\mathbf{R}_E$ ) in the plane formed by  $\mathbf{R}_E$  and the apparent velocity  $\mathbf{V}$ .

$$F_N = \frac{\rho}{2} V^2 A_{ref} C_N(\alpha, Re, M) \quad (62)$$

$$F_A = \frac{\rho}{2} V^2 A_{ref} C_A(\alpha, Re, M); \quad (63)$$

$$\mathbf{F}_A = -F_A \mathbf{R}_E \quad (64)$$

$$\mathbf{F}_N = F_N [\tau_R \times (\mathbf{R}_E \times \hat{\mathbf{V}})] \quad (65)$$

The torque vector equates to the rate of change of angular momentum, Eq. ???. These are the corrective torques, due to the normal aerodynamic forces; the damping torques and the roll torques.

$$eq : tqtot \dot{\mathbf{L}} = \tau = \tau_N + \tau_{da} + \tau_R \quad (66)$$

The normal force produces a rotational moment on the rocket since. This acts on the center of pressure  $X_{cp}$ , with a moment arm of  $\bar{X}$ , the stability margin (Eq. 67). The pitch damping torque ( $\tau_{da}$ ) includes both the aerodynamic damping and thrust damping. It is proportional to the angular velocity of the rocket.

$$\tau_N = F_N \bar{X} (\mathbf{R}_E \times \hat{\mathbf{V}}) \quad (67)$$

$$\tau_{da} = -C_{da} \omega \quad (68)$$

The roll torque can be both roll inducing and roll damping, the roll inducing torque in this case comes from the deflection of the ailerons.

$$\tau_R = \frac{\rho}{2} v^2 A_{ref} C_R d; \quad (69)$$

$$\tau_R = \tau_R \mathbf{R}_E \quad (70)$$

The simulation terminates when apogee is reached, i.e the vertical velocity is zero.

### 4.3 Simulation Outputs

The result of the solver comes as the state matrix and a time vector. This matrix is passed through the (`extract_data.m`) function, this function essentially re runs the state to log the desired flight variables through a logging function. The flight variables are not directly logged in the ODE45 solver because the solver can carry out multiple iteration at each time-step to reach a convergence criteria. In this case the logged variables will not be representative fo the final flight states.

The customisability of the simulator allows for any flight parameter to be logged and plotted. As a default; however, the trajectory, the height and various flight and stability parameter are plotted.

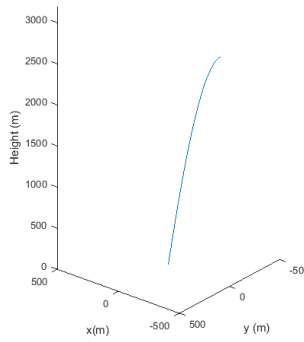


Figure 17: Left: 3 dimensional flight trajectory; Right: rocket height

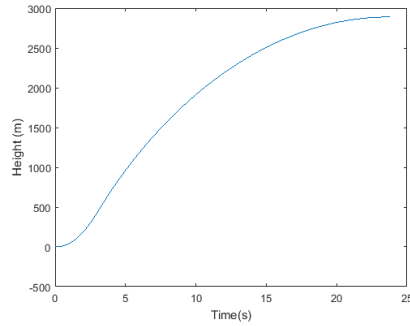


Figure 18: Left: 3 dimensional flight trajectory; Right: rocket height

In the flight information plots (Figure 19)  $C_D$  can be seen to reach a peak at the red vertical line. This corresponds to the motor burnout and corresponds to the peak velocity. This is to be expected as drag at higher velocities increases by the compressibility of air. Since all the propellant is burnt at this stage, the mass is constant from this point on. The angle of attack is very close to zero for much of the flight. Towards the end it increases as the rocket slows down and starts to bank, at this point the aerodynamic forces are not high enough to lower the angle of attack. This generally happens close to apogee.

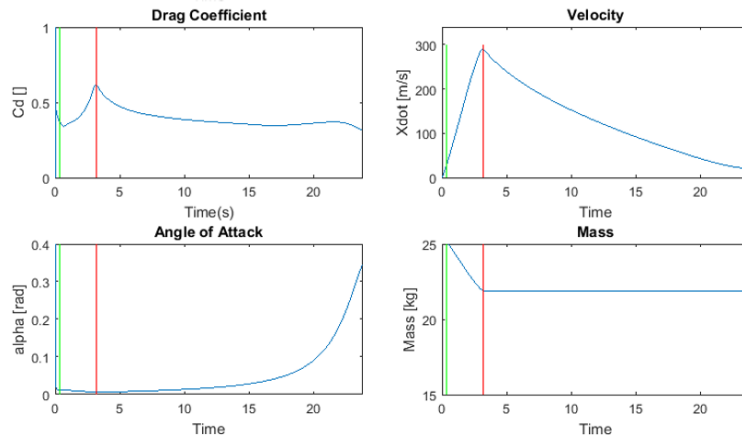


Figure 19: Left: 3 dimensional flight trajectory; Right: rocket height

Stability characteristics are shown in Figure 20. The stability margin should be greater than one

but not too high as mention in section 2. The damping ratio should be between 0.05 and 0.3, this has been recommended by Mandell [2] and come from rocketeering experience. In the stability margin plot the the effect of removing the lift correction is also plotted. The large deviation tells us that ignoring body lift is not a valid assumption for larger rockets.

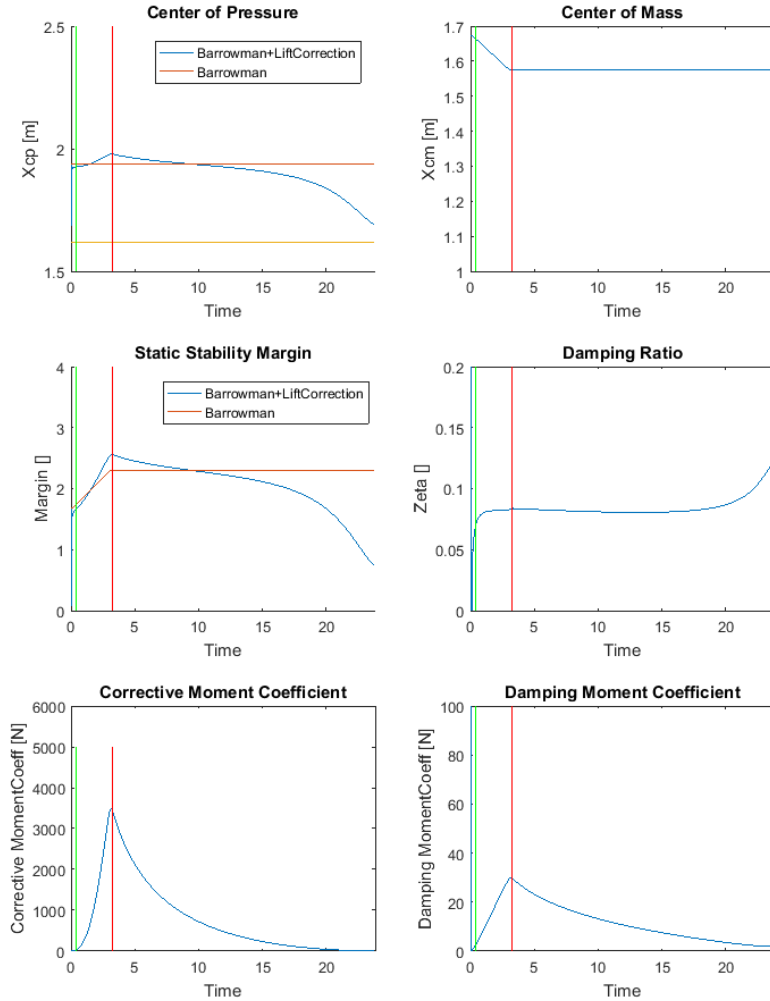


Figure 20: Left: 3 dimensional flight trajectory; Right: rocket height

#### 4.4 Comparison with RockSim

RockSim is the leading commercial simulator available for rocketeers to design rockets and plot trajectories. It has a easy to use GUI which gives users the ability to design rockets and simulate them under a verity of conditions.

The comparison done here is only between the resulting trajectories and flight characteristics of the 2 simulators. The same parameters as shown in Figure 14 were used to setup the simulation in both the simulators. The results are shown in Table 1.

Table 1: Comparison of the MATLAB simulator with RockSim

	MATLAB Simulation	RockSim
Height[m]	2889.3	3042.5
Max Velocity[ms <sup>-1</sup> ]	289	275
Rail departure velocity [ms <sup>-1</sup> ]	31.5	31.2
Time to Apogee[s]	23.83	24.82

The rail exit velocity, maximum velocity and the time to apogee are all quite similar. However, there is a noticeable difference in the maximum height achieved. Since the apogee height is the main judging criteria for IREC, it is important to know the cause of this difference. In RockSim there are 2 methods to calculate the normal forces, the Barrowman method and an custom RockSim method. Since there was no detail on how the RockSim method worked the Barrowman method was used. Rocksim does not account for the lift forces in the Barrowman method, this is compared to the MATLAB simulator in the stability margin plot in Figure 19. This factor, however, does not greatly effect the final height as the angle of attack is close to zero for much of the flight. The second, more major, difference is the  $C_D$  calculations of RockSim versus the MATLAB simulation shown in Figure 21.

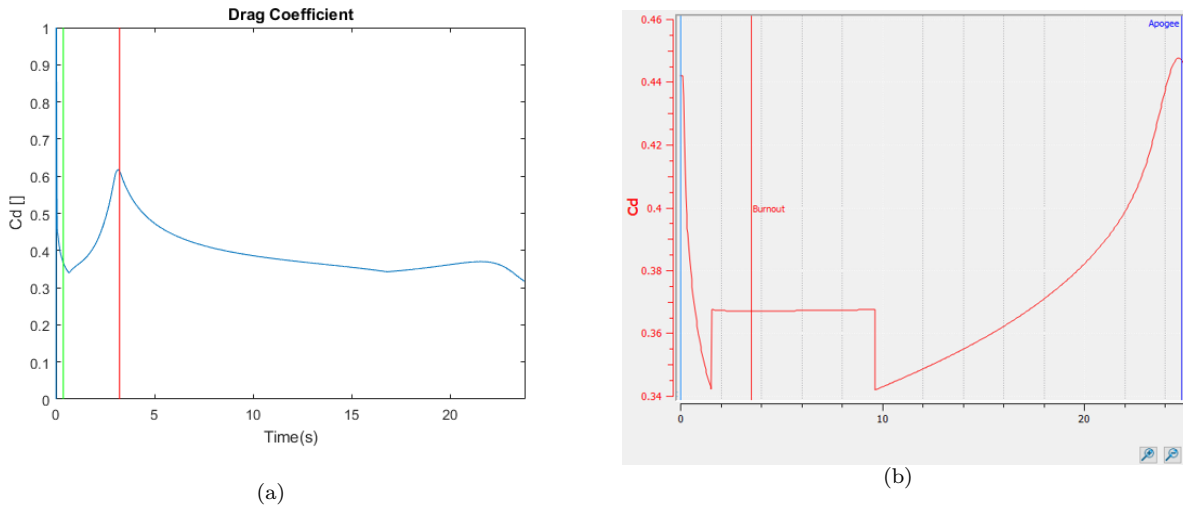


Figure 21: (a) The  $C_D$  as calculated in MATLAB showing a peak at motor burnout. (b) The  $C_D$  as calculated in RockSim, with the  $C_D$  cut off to approx. 0.363

In Figure 21(b) we can see that the  $C_D$  from RockSim simply cuts off past a certain velocity to a constant value. The reason for this is not clear, however, it has an effect of ignoring the effects from compressibility of air. A lower drag coefficient at higher velocity greatly reduces drag losses of the rocket resulting in a higher maximum height.

#### 4.5 Monte Carlo Simulation

The Monte Carlo method was applied to the simulator to account for the effect of uncertainty in parameter estimation. The methodology as described by Box [3] was used. The varied parameter is assumed to be normally distributed about the estimated value. As an example the stochastic  $C_N$  is given by Eq. 71.

$$C_N = C_N \xi(1, 0.1) \quad (71)$$

Where

$$\xi = N(1, \sigma^2) \quad (72)$$

A variance was attached to each parameter as listed in the Table 2. The simulation was run 30 times, in each run the parameters changes slightly according to the assigned variation. The resulting height of the simulations is plotted as a normal distribution (Figure ). The overall result from the simulation is presented as a scatter plot of apogee heights in Figure

Table 2: Variance of the stochastic parameters

Parameter varied	Variance ( $\sigma^2$ )
$C_N$	0.1
$C_A$	0.2
$X_{cp}$	0.05
Wind	3

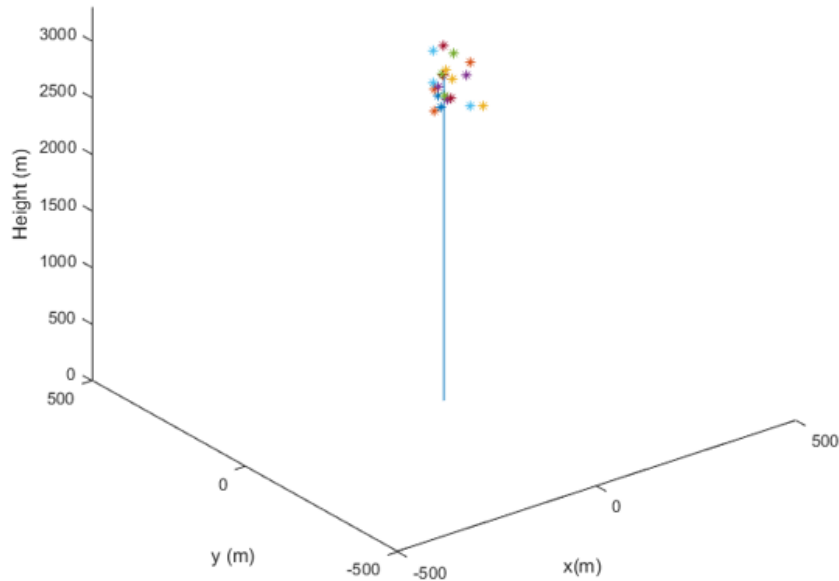


Figure 22: The line represents the trajectory of the non stochastic flight, each dot represents apogee of the stochastic simulation

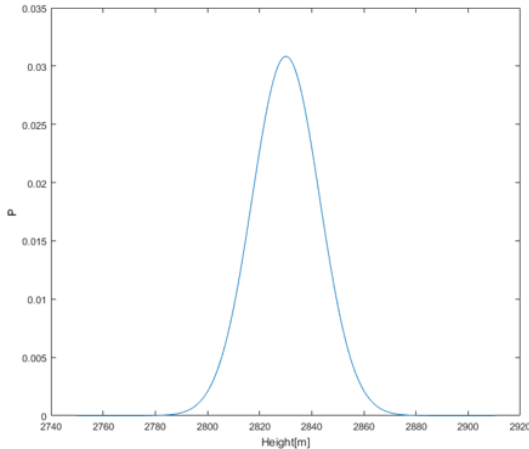


Figure 23: Height distribution plotted as a Gaussian  $N(2831.3, 163.2)$ , a slightly different weight configuration was used for the Monte Carlo simulation thus the lower mean height

A more interesting application of this method would be to check the probability distribution of the height as a result of only varying one parameter at a time.

## 5 Modified Tethys with control Surfaces

In order have a better understanding of the response of a rocket with active control surfaces it was decided to modify a small level 1 rocket with ailerons and air brakes. The kit chosen for this is the Tethys since it had a similar form to RORO1. Due to the structure of these level 1 kits the modifications were not straight forward. It was also important to keep the center of mass of the rocket in roughly the same location and not increase the weight of the rocket by much.

The ejection system of the Tethys is based on a time delay. After motor burnout there is a pre-configured delay, after this delay an explosive charge fires. The charge pushes a piston through the central part of the tube, causing pressure build up in the chamber and in turn pushing the cone and the parachute out (Figure 24). Due to this configuration no modifications can be made to this part of the rocket. The only available space is the nose cone and the lower section, where the rocket motor fits and the fins are attached. The lower section does not have a lot of space and is the load bearing part. The 54mm motor ("mothertube") is concentrically attached inside the 102mm body tube, the internal area between these tubes is where any components can be placed. The fins are epoxied onto this 54mm tube and the main body tube to carry the load from the motor to the rest of the body. In any modification the load bearing capacity of this connection has to be preserved.

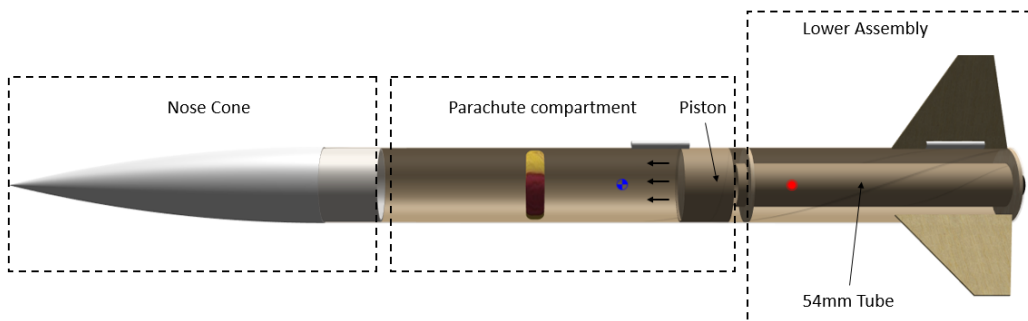


Figure 24: Tethys internal layout, the black arrows mark the direction of the piston movement after the ejection charge is triggered.

Fins are a simple way to control attitude, an ideal place to put them would be the nose cone as canards. This would avoid the modifications in the load bearing lower section. Canards cause a destabilizing moment, but this can be countered by increasing the main fin size. The main drawback of canard is that they can inverse roll control at certain velocity due to canard fin-coupling. In an inverted control scenario, a canard input to roll clockwise would make the rocket roll anti clockwise. The canards channels the flow over the main fins at the bottom increasing the pressure on the opposite side of the desired roll and inducing the anti-clockwise roll. Thus, it was decided to modify the current main fins and add ailerons.

The simplest method to implement braking is to have surfaces extend out from the rocket main body and increase the drag. However, braking surfaces also produce a normal force. For this moment to be stabilizing the brakes have to be placed below the center of mass. Secondly, they have to be placed such that they do not disturb the airflow over the main fins. With these restrictions in mind the brakes would be placed in the lower section as far from the fins space-permitting. This is right under the dry  $X_{cm}$ , where any normal force produced by the rocker will have a small effect on the overall normal moment.

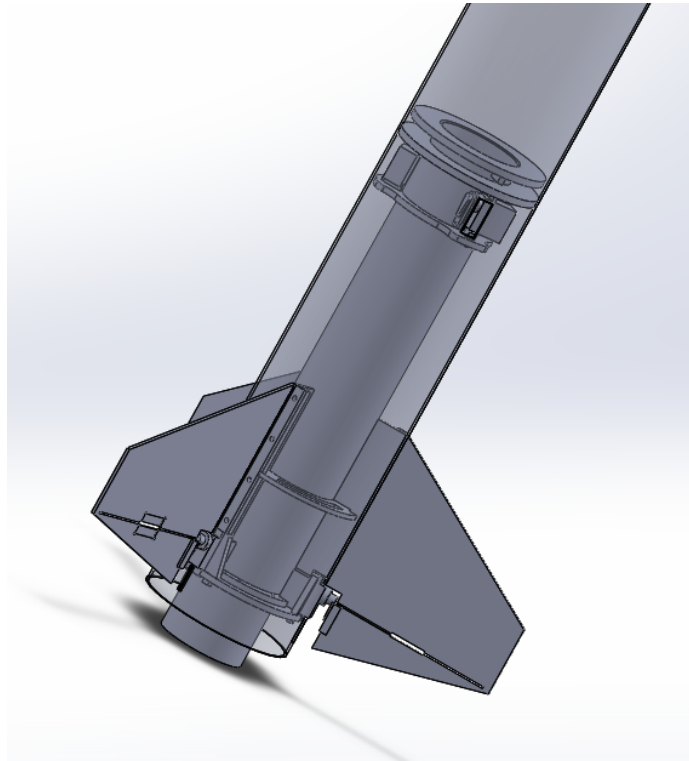


Figure 25: CAD model of the lower assembly

A detailed CAD model of the rocket body and lower assembly was produced to be able to appropriately modify this section (Figure 25). For both the brakes and ailerons it was important to choose the right servos to be able to fit in the thin lower section and have high enough torque to resist the air flow. S0009, 9g servos were chosen. The size and the torque values were appropriate for the application. However, they are relatively cheap servos, the choice of these specific servos was driven more from their availability than anything else.

## 5.1 Ailerons

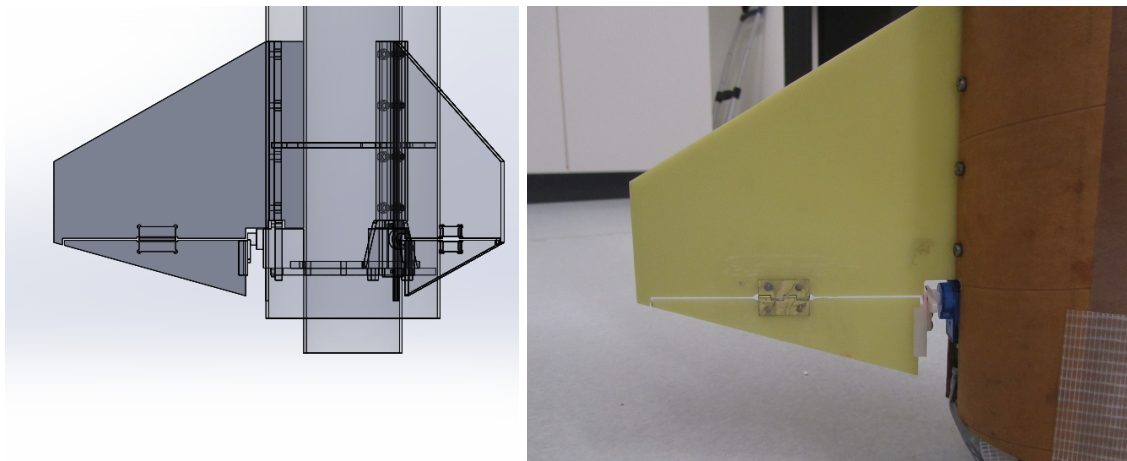


Figure 26: Fin layout in and actual implementation

The designed layout for the fins is shown in Figure 26 . The ailerons are machined from the fiber glass fins provided by the kit. To be able to machine them accurately a wooden template was first machined, on which the fins were fixed and the aileron sections cut (Figure 27). The hinges used to connect the two sections were simple off the shelf parts. The hinges were positions on the fins by a pre-cut pocket of the same size. and attached using pin covers with a layer of epoxy an fiber-glass cloth.

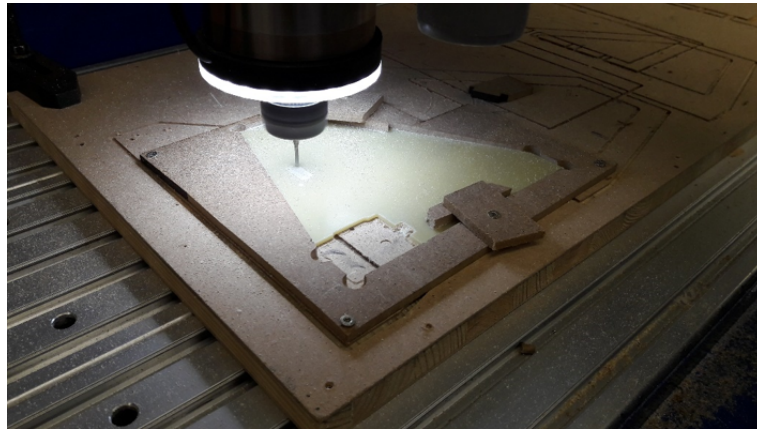


Figure 27: Servo attachment and coupling

The axial of the servos face radial outward. These are joints to the fin via plastic coupling (Figure 28). Since the ailerons are already connected to the main fin by a hinge joint. The couplings were not rigidly attached to the fins, such that the joint will not be over constrained. The fins simply slot into the coupling grooves.

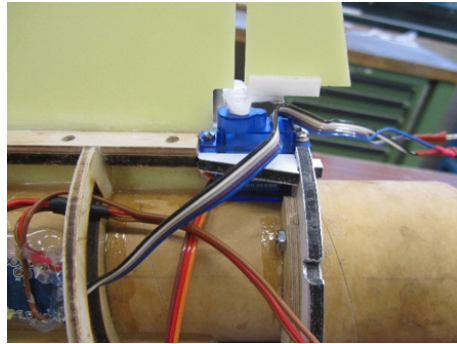


Figure 28: Servo attachment and coupling

## 5.2 Airbrakes

The air brakes are surfaces made by thermoforming PET around the main body tube to get the right shape. The hinges are attached to the braking surface using the same method as described for the ailerons. These hinges are attached onto a wooden bulkhead in the rocket with nails (Figure ).

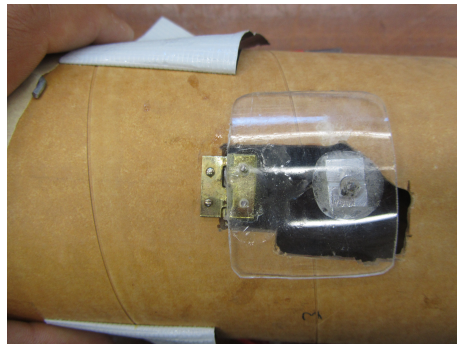


Figure 29: The brake plate attached to the rocket body

Each brake is actuated by a servo. A more effective design would have all the brakes mechanically coupled; however, this was not done due to the complexity of the design. The brakes are actuated through a two bar link mechanism (Figure) . For a 80 degree turn in the servo motor the brakes turn 50 degrees. The linkage also act as a force multiplier reducing the torque on the motor. Furthermore, the linkage auto locks when the 2 bars are straight ensuring the surfaces do not move under wind pressure.

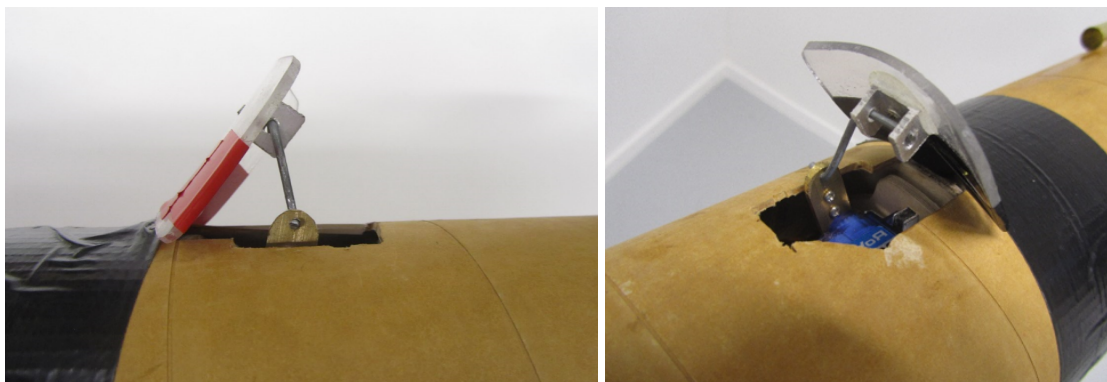


Figure 30: Left: Brake deployed with an actuation of 50 degrees: Right: Linkage configuration for the brake deployment

### 5.3 Electronics

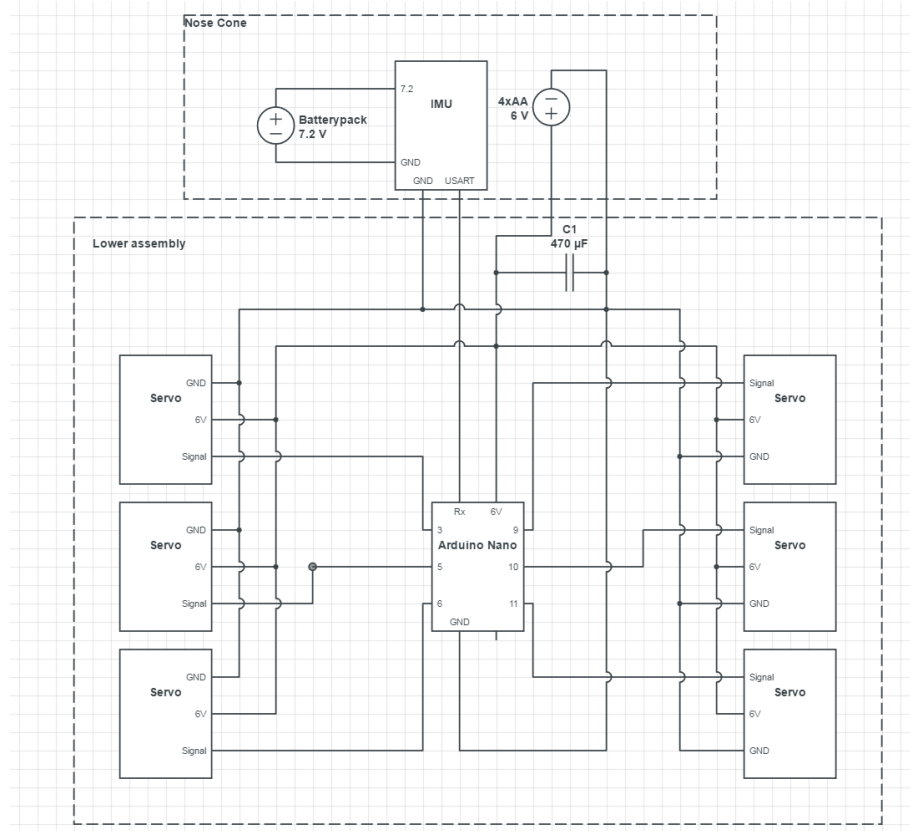


Figure 31: Circuit diagram for the electronic components

For space and mass distribution reason the two batteries, IMU and were fitted in the nose cone. The around was placed in the bottom assembly so it is closer to the servos. The connection between the cone and the bottom assembly was detachable since the cone separated during parachute ejection. Furthermore, the connection wires were attached outside the rocket to keep the piston area clear.

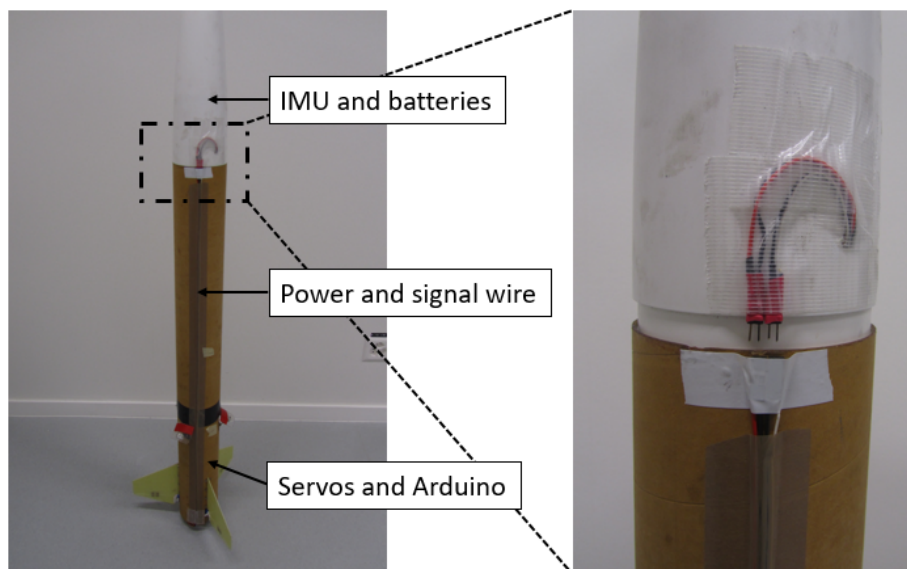


Figure 32: Location of the electronic components in the rocket, the zoomed in view to the right shows the connection which separates during parachute deployment

## 5.4 Structure

The simple structure was constructed inside the nose cone to securely hold the batteries and IMU (Figure 33). The lower assembly was designed such that it could be disassembled to access the components. Structural ribs were attached between the fins to improve rigidity of the structure. The ribs were laser cut and epoxied in place. Structural components with nuts were added on to the fins so they could be screwed on to the main body tube, for transferring the forces to the body.



Figure 33: Left: Modified nose cone with internal structure to hold the IMU module; Right: IMU module that can be slid onto the nose cone using 2 positioning rods

The structure to hold the braking servos and the aileron servos was machined from plywood, it is attached to the 54mm tube via epoxy. The brake linkage is made from brass and a steel rods (Figure 30 Right). The aileron servos structure was machined from plywood and aluminium di-bond. the Servo to fin coupler was machined from POM. The structure is screwed on to the 54mm tube can be slid off the tube if there is a need to replace the servos. The internal structure is shown in Figure 34.

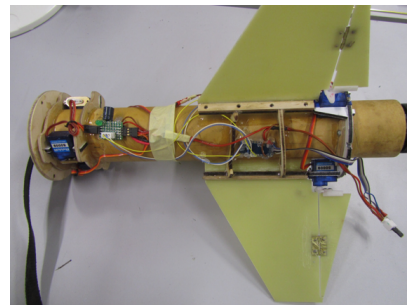


Figure 34: Internal support structure for the lower assembly components, the layout of the electronics and wiring can also be seen, hot glue was used to attach the electronic boards to the 54mm tube

The fin area was heavily reinforced to take the motor load, each fin is surrounded by 8 screws to a attach the lower assembly to the body tube (Figure 35).

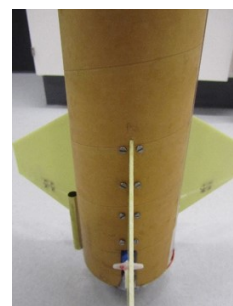


Figure 35: Attachment screws of the lower assembly to the body tube

## 6 Wind tunnel Testing

Wind tunnel testing for both RORO1 and Tethys was conducted at the Geneva Wind tunnel [17]. The tunnel has a  $2m \times 4m$  cross section and can generate wind velocities up to 300 kph. In order to test the rocket a rigid support structure, able to take the wind load and the weight of the rocket, was needed. The support structure was made out of aluminium profiles. Figure 36(a) shows RORO1 with the support structure. The intent of this structure was also to vary the angle of attack so that the center of pressure could be found. For the Thetys, the same structure was modified and can be seen in Figure 36(b).



Figure 36: (a) RORO1 with the support structure, rod in the middle of the support was used to change the angle of attack (b)Tethys with the support structure

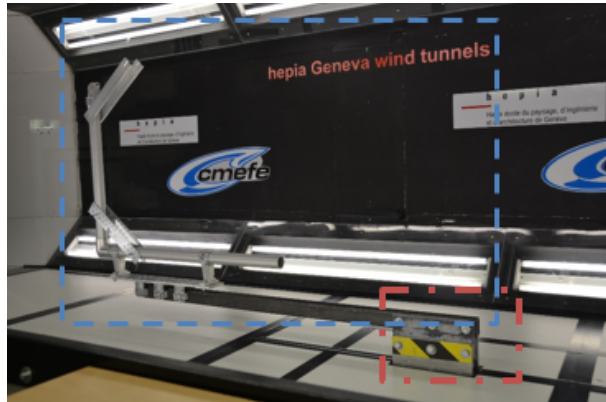


Figure 37: The Tethys support structure(blue) being tested for its drag contribution, 6 axis sensor (red)

The structure is attached to a 6 degree of freedom torque and force sensor. The forces induced by the wind on the rocket and the structure is measured by the sensor as seen in Figure 37. Unfortunately due to the lack of rigidity of the structure RORO1 was only tested up to 120 kph and Tethys was tested up to 150 kph. Furthermore, the test data for RORO1 was not very reliable. For the Tethys the control surfaces were tested at various speeds at constant temperature and pressure. Each data point is an average value of 60 readings recorded over 30 second.

Table 3: Data points collected at various velocities and configurations

Test Setup	Velocities [ $m s^{-1}$ ]	Surface Configuration [deg]
Rocket	21, 28, 35, 42	NA
Brakes	21, 28, 35	40, 60, 80
Ailerons	21, 28, 35	15, 30, 54
Structure	21, 28, 35, 42	NA

## 6.1 Brake test analysis

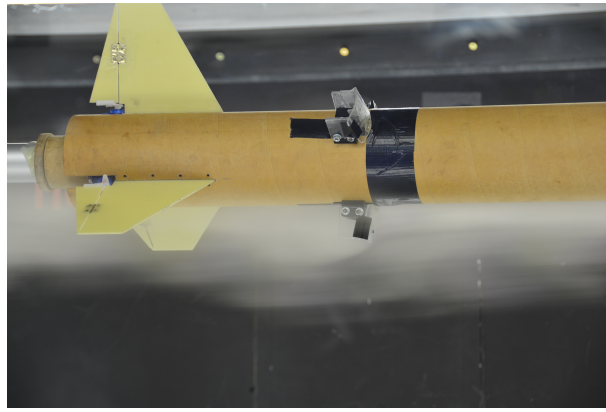


Figure 38: A smoke test is shown here to check the effect of brakes on the flow, specifically the disturbances over the fins. The brakes were set at the specified angles using machined wedges

Brake drag forces are obtained by removing the rocket and structure drag from the brake setup. Using the surface area of one plate as the reference area, the average drag coefficient of the brake at the deployed angle,  $C_{D\theta}$ , was calculated. This was inserted in Eq. 73 to get the  $C_{D0}$  for the plate, ie the drag it would face if it was perpendicular to the flow. If the model described in Section 3.5.1 was accurate, the resulting  $C_{D0}$  should be relatively constant for all brake configurations and flow velocities -close to the drag coefficient of a plate ( $C_D = 1.17$ ).

$$C_{D0} = \frac{C_{D\theta}}{\sin^3(\theta)} \quad (73)$$

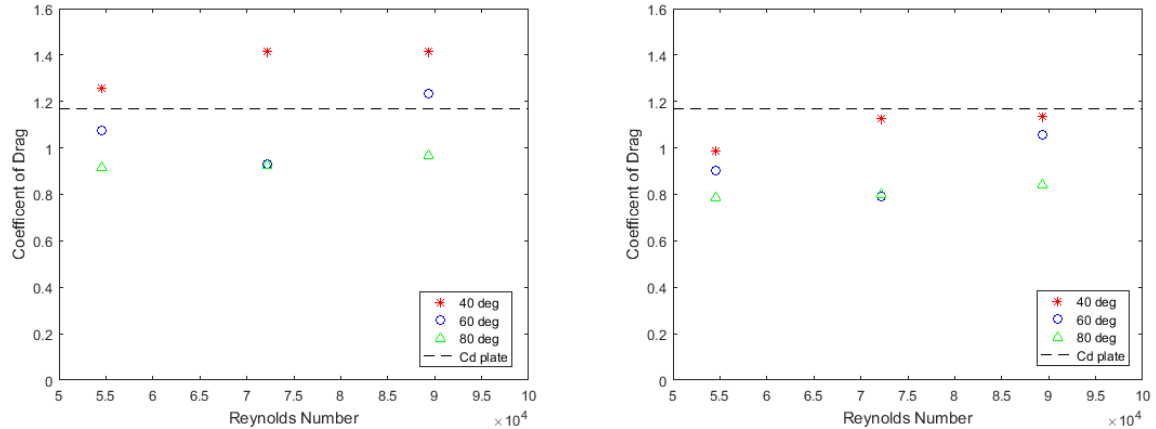


Figure 39: Right:  $C_{D0}$  calculated with out boundary layer correction; Left:  $C_{D0}$  calculated with boundary layer correction

The results can be seen in Figure 39. Initially no correction for the boundary layer interference was done. After noticing a slight trend with the Reynolds number the boundary layer correction was carried out. Even though the trend persists, the values are much closer together. The  $C_{D0}$  also show a trend with the actuation angle of the brake. This indicates that an underlying flow phenomena may be missing in the model. A correction for this, however, has not been done. Overall, it is considered that the actual  $C_{D0}$  of the brakes is the average of the test  $C_{D0}$  calculates at the 3 deflection angles and speeds. This is given by

$$C_{D0,brake} = 0.936 \quad (74)$$

This value is slightly smaller than the flat plate  $C_D$  of 1.17, this maybe be explained by the fact that the brake plates are not flat but curved surfaces.

## 6.2 Aileron test analysis



Figure 40: Aileron configuration to induce a roll moment

The ailerons were set to a roll inducing configuration for the wind tunnel testing. Aileron moments were obtained by removing the rocket and structure moments. The the roll moment generated was converted to the average lift generated by one fin by using the distance from the center to the mean aerodynamic chord ( $r + y_{MAC}$ ). The average lift coefficients at various deflection at the 3 test velocities are plotted in Figure 41.

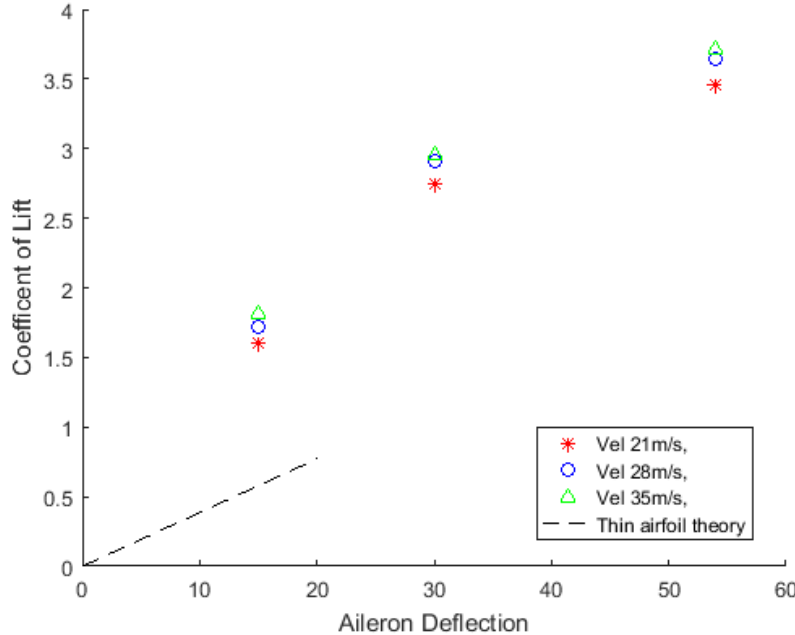


Figure 41: Wind tunnel data compared to theoretical results

The test results are compared to the lift generated according to the thin airfoil theory as detailed in Section 3.5.2. For the fins in Tethys, the aileron effectiveness and lift derivative is:

$$\frac{d\alpha}{d\eta} = 0.56 \quad (75)$$

$$C_{L_\alpha} = 3.88. \quad (76)$$

In Figure 41 this theoretical result is plotted as the dashed black line. The validity of the theory is only up to 15 degrees. In retrospect the test data should have been collected at much lower deflection angles to get a better comparison with the theory. The only value that can be truly compared is the 15 degree deflection. However, this is almost 3 times larger than that of the predicted value. This is a surprising result, especially since the thin air foil theory give an upper limited to fin lift [15]. The reason for this deviation has not been determined.

The desired outcome of this experiment would be to determine a factor to adjust the effectiveness ratio of the aileron to reflect the actual fin configuration in the rocket. Using the current data this correction factor is 3. The expected value was less than one. A more detail analysis was necessary to determine the validity of this correction.

## 7 Flight and Data Analysis

RORO1 and the Tethys were test launched on the 20 May 2017 at a launch site in Kaltbrunn, Switzerland. The apogee aim for RORO1 was around 600m due to the height restriction on flight. For Thetys open loop braking was tested, ailerons were not tested here due to safety concerns in case of failure.



Figure 42: (a) RORO1 flight test (b)Tethys flight test; rockets just after launch rail exit

## 7.1 RORO test flight

The apogee achieved for RORO1 was 504m taken from the barometer and 508 meters taken for the recovery electronics used to deploy the parachute. This is much lower than the apogee predicted by the simulation which was 616 meters. As RORO came off the launch rail, it faced a relatively strong angular perturbation which caused the rocket to bank strongly towards one side, and then flip to the other when the correcting forces got big enough. This oscillation quickly died down after the motor burn.

In order to analyze the cause of the oscillation the 6 DoF IMU data was analysed. The IMU used only provided raw unfiltered data and had to be processed to extract usable information. The accelerometer had to be corrected for biases. The gyro was calibrated using the 40 sec before launch when the rocket was stationary on the rail. Repeated values of the data were removed. The launch angle of the rocket was calculated using the gravity acceleration as read by the accelerometer. Since the IMU was not placed exactly at the center of mass of the rocket. The acceleration data had to be transformed in order to account for the centrifugal forces. This transformation also has to take into account the shifting center of mass of the rocket during motor burn.

Next, the acceleration data was passed through the Savitzky-Golay filter. This filter smooths the data using a polynomial of a specified order without introducing a delay. This function is present in the MATLAB signal processing tool box. The gyro rates were differentiated to get the angular accelerations, these were also passed through the Savitzky-Golay filter to reduce the noise.

The angular rate data was converted into quaternion rates and using the initial orientation, the quaternion rates were integrated throughout the rocket flight to get the attitude of the rocket in quaternions. A rotation matrix at each sample time of the data was calculated using the quaternion orientations, and the accelerometer data was converted to the earth reference frame. After removing the effect of gravity the data was integrated to get the flight velocity and position of the rocket. This trajectory is displayed in Figure 43, the angular accelerations are displayed in Figure 44.

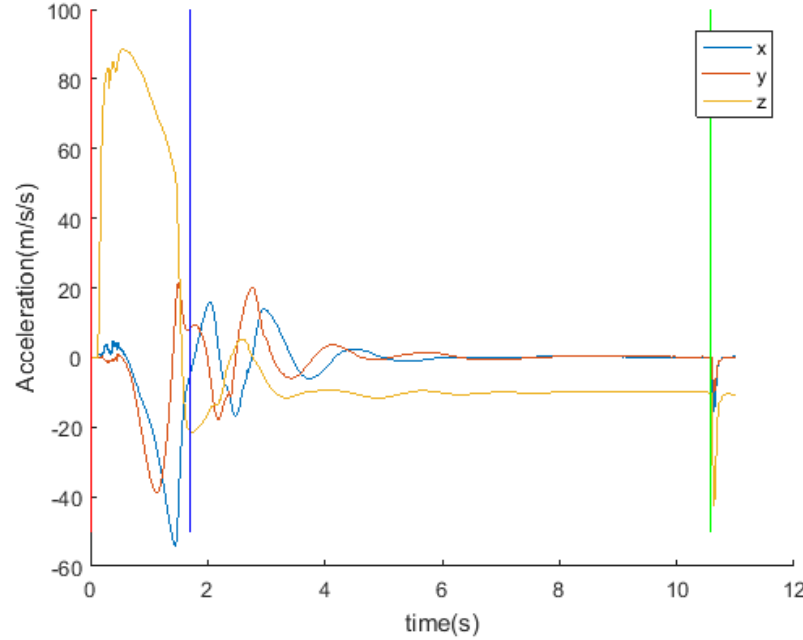


Figure 43: Accelerated of RORO1 during launch in the earth reference frame

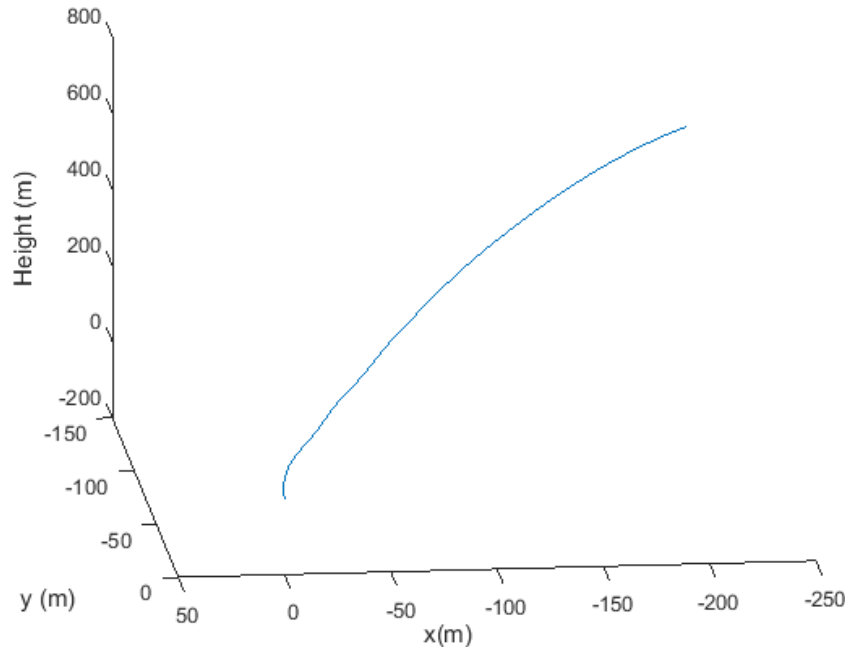


Figure 44: Trajectory of RORO1 as calculated using IMU data, note: x,y and the z axis are not the same scale, blue vertical line marks motor burnout, green line is separation

The maximum height as calculated by the IMU was 608 meters, even though this is closer to the simulator, it is incorrect due to the drift of the gyro. One way to correct this drift was to use the magnetometer data. However, the magnetometer was not properly calibrated and could not be used.

Even though we cannot get the absolute trajectory from the IMU data looking at the angular accelerations (Figure 43), the moment can be seen peaking around 1.5 seconds. The moments quickly dampen after burn out. These oscillations can also be seen in the trajectory plot (Figure 44). These oscillations are the reason a much lower height than the simulation was achieved. The leading hypothesis

for the cause of these oscillations is a combinations of low aerodynamic correcting moments, since the fins were designs for a much higher rail exit velocity and thrust misalignment as the rocket is seen to be accelerating sideways during a low angle of attack.

It was decided to increase the fin side to counter this so the rocket would have slightly higher stabilising moments -even at lower speeds.

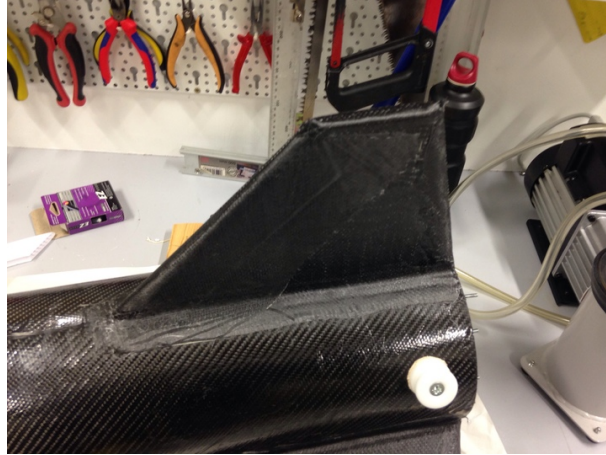


Figure 45: Final fins with span increased by 50mm

## 7.2 Tethys test flight

The intent of this launch was to test the response of the rocket when the air brakes are actuated mid flight. The brakes were deployed at a certain time after launch. The barometer data from the nose cone was passed to the arduinio. After a 15 m vertical height gain a 5 second timer in the arduino was turned on. At the 5 second mark the brakes were deployed to an angle of 50 degrees.

The flight was relatively stable. The most relevant parameter in this case is the acceleration in the roll axis detection in the frame of the rocket, since the brakes are attached to the rocket. The IMU data was extracted from the rocket using similar procedures as for RORO.

The roll axis acceleration data was compared with the simulation data. In the simulation, the brake is modelled as an increase in  $C_D$  when the brakes are deployed the value used for the brake  $C_D$  is the one calculated from wind tunnel testing. The deployment conditions are the same as the test rocket. Since the flight of the rocket was relatively straight the normal forces of the brakes are ignored. The comparisons between test flight and simulation are shown in Figure ???.The biggest difference is seen during burn, indicating that the thrust curve is not very accurate. The deceleration after burnout is very similar, indicating that the aerodynamic drag from the simulation model is representative of the experiential situation.

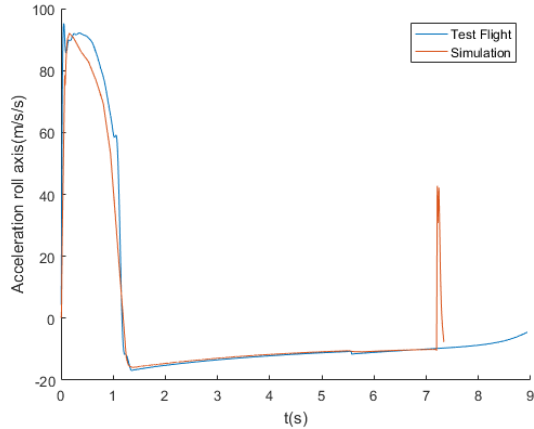


Figure 46: Comparison of the simulation and test flight, the peak in test flight data at 7.2 sec is the rocket separation

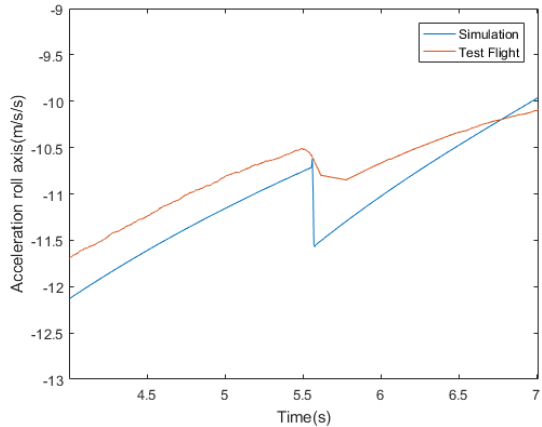


Figure 47: Zoomed plot from Figure 46 showing the axial deceleration comparison of the simulation and the flight test at brake deployment

In Figure 47 we can see the increase in deceleration due to the brake. The magnitude and especially timing are very close between the simulation and test flight. The simulation deceleration is a jump as the  $C_D$  increase due to brakes is instantaneous.



Figure 48: Deployed brakes during Tethys flight can be seen as bumps on the rocket surface

Table 4: Simulator and test flight height

	Simulation	Test Flight
Height [m]	345	313

The height from the simulator and the barometer is compared, the difference may come from the fact that the exact wind velocity was and the rail launch angle is not known. Secondly, the rocket has lot of external features like the wires and the brake plates at zero deflection that cause drag.

It is to be noted that deployment of the brakes in the flight test was too late to have any significant effect on the final apogee of the rocket. According to the simulator the height reduced only by 5[m] from the apogee achieved without the brakes. If the same brakes were actuated right after motorburn out at 1.3[s] the reduction in height would be 50[m]

## 8 Conclusion

This project builds a strong base for future simulation and control projects for model rocket. It is also a good starting point for anyone looking to understand the dynamics of subsonic rocket flight. The aerodynamic forces are models in detail using semi empirical methods. Any further detail would require data specifically collected from model rockets.

The simulation built is tailored specifically for future IREC or similar competitions, where the user has detailed information on the masses and inertias of the rocket. Detailed documentation is provided, in the form of this report to help the user understand the inner workings of the rocket, and the modularity of the simulator means that other models can be integrated to the simulation.

A major contribution of this simulator over what is widely available is the modelling of the control surfaces. A basic Monte Carlo simulation is done; however, in the future this could be improved further to understand the effect of each stochastic parameters on the rocket individually. The brake model has been validated through wind tunnel and flight testing. Further brake simulations can be done to understand the best time to apply the brakes. For the ailerons some more work would be needed to consolidate wind tunnel data with theory and finally carry out flight test to validate the model.

The modified Tethys rocket built can be used as a test platform for further collection of data and eventually for the testing of controllers. The ailerons are well built although the brake surfaces can be replaced with more accurate parts. The servo motors used are not of a high quality and it is recommended that for future testing these be replaced with better servos.

Even though the wind tunnel provided useful information, a better test fixture could have greatly increased the amount of data. For the future more effort should be put in to developing test stands for similar purposes. Further identification for aerodynamic parameters can be done through CFD. A simple CFD model was developed which simulates the rocket body at Mach 0.6. The results were similar to the semi-empirical aerodynamic models. However, further development of this model is required to get usable data.

The simulator can be further tuned through flight data. Parametrised equations which are functions of rocket variables like, angle of attack, Reynolds number and Mach number can be added to the equations for  $C_A$  and  $C_N$ . The parameters of these added equations can be tuned such that the simulator matches the test flight more closely. This tuning can be done through various optimisation methods, such as least square minimisation of the error between test flight and simulation.

The two launches provide valuable data to improve the simulation. However, the IMU data has to be corrected for sensor drifts, this can be done thoroughly using a calibrated magnetometer and filtering

the date by using e.g.the Kalman filter. Getting better state estimates of the model rocket flight using such filters is vital for both tuning the simulation and eventually controlling the rocket.

The simulator can only model liner wind profiles at the moment, better wind modelling would greatly improve the reliability of the simulator. Overall, the simulator is seen as reliable and will be used in the IREC 2017 competition to predict the apogee of the rocket.

## References

- [1] Barrowman, J.A., *Theoretical Prediction of the Center of Pressure*, Camebridge, 1966.
- [2] Mandell, G., Caporaso, G., Bengan, W., *Topcis in Advanced Model Rocketry*, NARAM-8, 1978.
- [3] Box, S., Bishop, C. Hunt, H., *Estimating the dynamic and aerodynamic paramters of passively controlled high power rockets for flight simulaton*, 2009.
- [4] Box, S., Bishop, C. Hunt, H., *Stochastic Six-Degree-of-Freedom Flight Simulator for Passively Controlled High-Power Rockets*, Journal of Aerospace Engineering, Vol. 24, No. 2, 1990, pp. 31–45,2011.
- [5] Gelejs, R., *Wind Stability - What Barrowman Left Out*, 1998.
- [6] Niskanen, S., *Development of an Open Source model rocket simulation software*, M.Sc. thesis, Helsinki University of Technology, 2009. Available at <http://openrocket.sourceforge.net/documentation.html> Accessed: 2017-06-09
- [7] *U.S Standard Atmosphere*, 1976.
- [8] ARGOS, Advanced Rocketry Group of Switzerland.<http://www.argoshpr.ch/j3/> Accessed: 2017-06-09
- [9] Thrust Curve Hobby Rocket Motor Data <http://www.thrustcurve.org/> Accessed: 2017-06-09
- [10] Diederich, F., *A plan-form parameter for correlating certain aerodynamic characteristics of sweepings*, NACA-TN-2335, 1951
- [11] George M. Siouris, *Missile Guidance and Control Systems*, Springer- 2004
- [12] Louis d, Duncan and Ronald j. Ensey, *Six Degree of Freedom Digital Simulation Model for Unguided fin-Stabilized Rockets*, ERDA-196 1964
- [13] Hannes Bleuler, 1954- ; Reymond Clavel, 1950- ; Roland Siegwart, 1959- ; 2001. *Robotique, micro-robotique : pour la section de microtechnique 2ème cycle TPr Nouv. éd.*, octobre 2001
- [14] Hoerner, S. F. (1965). *Fluid-dynamic drag: practical information on aerodynamic drag and hydrodynamic resistance* Midland Park, NJ: Hoerner Fluid Dynamics.
- [15] Hoerner, S.F. and Borst, H.V., 1985. *Fluid-dynamic lift: practical information on aerodynamic and hydrodynamic lift*. Hoerner Fluid Dynamics; 2nd edition
- [16] H. Schlichting, *Boundary Layer Theory* McGraw-Hill, New York, 1979, p. 638.
- [17] Research Group for Fluid Mechanics, *Haute École du paysage, d'ingénierie et d'architecture de Genève* <http://cmefe.ch/>
- [18] Intercollegiate Rocket Competition <http://www.soundingrocket.org/2017-irec.html>